Classification of fragile topology enabled by matrix homotopy

Ki Young Lee [1,*] Stephan Wong [1] Sachin Vaidya [2] Terry A. Loring [3] and Alexander Cerjan [1,†]
[1] Center for Integrated Nanotechnologies, Sandia National Laboratories, Albuquerque, New Mexico 87185, USA
[2] Department of Physics, Massachusetts Institute of Technology, Cambridge, Massachusetts 02139, USA
[3] Department of Mathematics and Statistics, University of New Mexico, Albuquerque, New Mexico 87131, USA

(Received 5 March 2025; accepted 21 August 2025; published 10 September 2025)

Flat bands in twisted materials have attracted considerable attention due to the emergence of correlated phases that can be associated with the non-Wannier-representable nature of its single-particle states. Specifically, these bands can exhibit a class of topology that can be nullified by the addition of trivial bands, termed fragile topology, which has required an expansion of prior classification schemes. However, existing approaches for predicting fragile topology rely on momentum-space methods, e.g., Wilson loops, presenting a fundamental challenge for using fragile topology as a predictor of correlated phases in aperiodic systems, such as incommensurate twist angles in moiré materials. Here, we develop a $\mathbb{Z}_2$ energy-resolved topological marker for classifying fragile phases using a system's position-space description, enabling the direct classification of finite, disordered, and aperiodic materials. By translating the physical symmetries protecting the system's fragile topological phase into matrix symmetries of the system's Hamiltonian and position operators, we use matrix homotopy to construct our topological marker while simultaneously yielding a quantitative measure of topological robustness. We demonstrate our framework's effectiveness in both a low-energy tight-binding model and a continuum photonic crystal model of $C_2\mathcal{T}$-symmetric systems, and find that fragile topology can both persist under strong disorder and even exhibit disorder-induced reentrant phase transitions. Our photonic crystal results also demonstrate the robustness of fragile topology, and the applicability of our approach, to heterostructures lacking a bulk spectral gap. Overall, our framework serves as an efficient tool for elucidating fragile topology, offering guidance for the prediction and discovery of correlated phases in both crystalline and aperiodic materials.

DOI: 10.1103/5rqd-bp11

I. INTRODUCTION

Since their discovery, topological phases of matter have served as pivotal physical properties that broaden the frontiers of functional materials, both through their protection of boundary-localized states and through their prediction of delocalized single-particle wave functions that can precipitate correlated phases. Representative examples include Chern insulators [1] and topological insulators [2], which host gapless edge states protected by associated topological invariants and persisting as long as their internal symmetries are preserved and the corresponding spectral gap remains open. Such classes of topology are now referred to as strong and exhibit a bulk-boundary correspondence, linking the presence of protected boundary states to the nonzero topological indices of the bulk bands. Likewise, in conjunction with certain types of interactions, the delocalized electrons in topological bands can give rise to correlated phases such as fractional Chern insulators [3–8] and superconductivity [9–11]. Within a K-theoretic framework [12–14], classification schemes rooted in vector bundles can systematically assign topological indices to band gaps by summing up the topological invariants of each occupied band.

Recently, the emergence of crystalline-symmetry protected topological phases [15–17] has revealed a richer variety of phenomena including weaker forms of topology. Distinct from strong topology, crystalline topology has a nuanced bulk-boundary correspondence [18–21], stimulating the development of theoretical frameworks such as topological quantum chemistry [22], symmetry indicators [23,24], and Wilson loop approaches [25,26] for classifying these subtle phases. Among these weak topological phases, the concept of fragile topology [18] has been found as a contrasting case to stable topology, where the topological features of certain bands can be trivialized through the addition of atomic limits. Importantly, the moiré flat bands of small-angle twisted bilayer graphene (TBG) [11,27–34] have been identified as possessing such fragile topology, indicating the delocalized nature of its single-particle wave functions and attracting significant attention due to potential connections to correlated phases [35–38] and superconductivity [39–43]. This class of topology also appears relevant to debates regarding the weak topological protection [44–47] of the interface states

*Contact author: kiylee@sandia.gov
†Contact author: awcerja@sandia.gov

observed in various photonic crystal (PhC) platforms, as well as to potential applications of corner states and some types of edge states [48–56]. However, existing studies of fragile topology have focused on momentum-space classifications [18,28,30,57–60], prohibiting the application of these approaches to aperiodic and disordered materials. In particular, the lack of a position-space approach for classifying fragile phases that works with finite regions of a material inhibits the ability to study the manifestation of such topology for twist angles near a magic angle. Such an approach could provide insight into how delocalization of a system's single-particle wave functions occurs, and thus how correlated phases appear.

Here, we derive and demonstrate a position-space approach for classifying fragile topology and find an associated measure of robustness. Specifically, we show how the physical symmetries that protect fragile topology can give rise to matrix symmetries in a system's Hamiltonian and position operators when expressed in an atypical basis. These matrix symmetries can then be used to define a homotopic invariant that distinguishes two-dimensional (2D) systems based on which atomic limit they can be continued to, yielding an energy-resolved $\mathbb{Z}_2$ topological marker. Moreover, this approach implicitly introduces a quantitative measure of topological protection that remains valid under a variety of conditions, including finite system size, disorder, and environmental perturbations. We apply our approach to a disordered $C_2\mathcal{T}$-symmetric TBG model and a 2D photonic crystal embedded in an air background, showing that fragile topology can persist even under strong disorder and when a heterostructure lacks a bulk spectral gap. Our disordered simulations also reveal a disorder-induced reentrant transition [61,62] to a fragile phase with increasing disorder strength. Altogether, as our work shows how to characterize fragile topology beyond momentum-space descriptions, it may offer insights into both natural and metamaterial aperiodic and moiré systems, as well as correlated phenomena and superconductivity. In addition, the arguments we present here provide guidance on how to develop further position-space topological classification approaches for predicting forms of material topology associated with delocalization.

II. POSITION-SPACE ENERGY-RESOLVED MARKER FOR FRAGILE TOPOLOGY

We start by deriving an energy-resolved $\mathbb{Z}_2$ marker that classifies fragile topology in finite $C_2\mathcal{T}$-symmetric systems, with $\mathcal{T}^2 = \mathbf{1}$ and without requiring the system to have either symmetry in isolation. The key difference of our approach is that rather than focusing on a system's eigenstates, as are used in standard classification methods for fragile topology such as Wilson loops [25,30,32,52,55,63,64], our framework is instead rooted in the system's operators directly, such that these eigenstates never need to be determined. By definition, the Hamiltonian of a $C_2\mathcal{T}$-symmetric 2D system obeys

$$(C_2\mathcal{T})^{-1} H (C_2\mathcal{T}) = H, \tag{1}$$

while the system's position operators X and Y anticommute with this symmetry due to C_2,

$$(C_2\mathcal{T})^{-1} X (C_2\mathcal{T}) = -X, \quad (C_2\mathcal{T})^{-1} Y (C_2\mathcal{T}) = -Y. \tag{2}$$

This suggests that we should define a "symmetry-informed, transposelike" matrix operation ρ as

$$M^\rho = (C_2\mathcal{T})^{-1} M^\dagger (C_2\mathcal{T}) = C_2 M^\top C_2; \tag{3}$$

see Appendix A 2 for the simplification. In other words, this operation is the transpose intertwined with a rotation, and associates the system's physical $C_2\mathcal{T}$-symmetry to a set of mathematical matrix symmetries for its operators as

$$X^\rho = -X, \quad Y^\rho = -Y, \text{ and } H^\rho = H. \tag{4}$$

The relations in Eq. (4) are reminiscent of the system's operators being either symmetric $M^\top = M$ or skew-symmetric $M^\top = -M$, which in general are useful properties for studying matrix homotopy. For example, two invertible Hermitian skew-symmetric matrices M_0 and M_1 are homotopy equivalent and can be connected via a path of invertible Hermitian skew-symmetric matrices M_t with $t \in [0, 1]$ if and only if $\text{sign}[\text{Pf}(M_0)] = \text{sign}[\text{Pf}(M_1)]$, where Pf denotes the Pfaffian. This is because the Pfaffian can only change sign when two of eigenvalues of some M_t simultaneously cross 0, at which point the connecting matrix $M_{t'}$ would be noninvertible (see Remark A 2 in Appendix A 4 and Sec. 3.9 of Ref. [65]).

The key reason to define ρ is that if ρ commutes with the adjoint, such that $(M^\rho)^\dagger = (M^\dagger)^\rho$, there is a basis in which $\rho \to \top$ (see Appendix A 2). Thus, if possible, this single step allows one to link the system's essential physics, contained in ρ, to prior mathematical results on matrix homotopy, enabling the definition of a topological invariant. Here, one can directly compute that

$$(M^\rho)^\dagger = C_2 \left(M^\top\right)^\dagger C_2 = C_2 \left(M^\dagger\right)^\top C_2 = \left(M^\dagger\right)^\rho,$$

and that the unitary matrix

$$W = \frac{1}{\sqrt{2}} (C_2 + i\mathbf{1}) \tag{5}$$

transforms the system to the basis in which $\rho \to \top$. Specifically, this means that

$$(WXW^\dagger)^\top = -WXW^\dagger, \quad (WYW^\dagger)^\top = -WYW^\dagger,$$
$$\text{and } (WHW^\dagger)^\top = WHW^\dagger. \tag{6}$$

To develop an invariant to classify fragile topology protected by $C_2\mathcal{T}$ symmetry, we combine the system's operators centered about a choice of (x, y, E) in position-energy space using the Pauli matrices $\sigma_{x,y,z}$:

$$\begin{aligned} &L_{(x,y,E)}(WXW^\dagger, WYW^\dagger, WHW^\dagger) \\ &\quad = \kappa (WXW^\dagger - x\mathbf{1}) \otimes \sigma_x + \kappa (WYW^\dagger - y\mathbf{1}) \otimes \sigma_z \\ &\qquad + (WHW^\dagger - E\mathbf{1}) \otimes \sigma_y, \end{aligned} \tag{7}$$

yielding a spectral localizer [66–69]. Here, κ is a scaling coefficient that sets the spectral weight of the position operators relative to the Hamiltonian. In spectrally gapped systems, κ is typically on the order of $\kappa \sim E_{\text{gap}}/L_{\min}$, where E_{gap} is the

width of the gap and $L_{\min}$ is the minimum length of the system in any direction [68]. Heuristically, the use of the Pauli matrices is enabling us to define a single matrix $L_{(x,y,E)}$ using the system's operators while preserving the independence of the information carried in X, Y, and H, in an analogous manner to how the Pauli matrices (along with $\mathbf{1}$) form a complete basis for 2×2 Hermitian matrices.

The critical features of Eq. (7) are that it is Hermitian for any (x, y, E), and at $x = y = 0$ (i.e., the center of rotation), $L_{(0,0,E)}$ is skew-symmetric. This skew symmetry has been achieved by placing $WXW^\dagger$ and $WYW^\dagger$ against σ_x and σ_z, and placing $WHW^\dagger$ against σ_y, such that each tensor product is between a symmetric matrix and a skew-symmetric matrix (as $\sigma_{x,z}^\top = \sigma_{x,z}$ while $\sigma_y^\top = -\sigma_y$). Thus, the energy-resolved invariant

$$\zeta_E(X, Y, H) = \text{sign}[\text{Pf}(L_{(0,0,E)}(WXW^\dagger, WYW^\dagger, WHW^\dagger))] \tag{8}$$

distinguishes systems that can be connected to each other while preserving $C_2\mathcal{T}$ symmetry and maintaining a positive local gap

$$\mu_{(x,y,E)}(X, Y, H) = \min(|\text{spec}[L_{(x,y,E)}(X, Y, H)]|), \tag{9}$$

where spec$[M]$ is the spectrum of M. By definition, $\zeta_E \in \{-1, +1\} \cong \mathbb{Z}_2$; if $\zeta_E = -1$, the system at E cannot be connected to a trivial atomic limit, and vice versa. Moreover, since ζ_E cannot change its value without $\mu_{(0,0,E)} \to 0$, either by changing the choice of E or by perturbing the system, the local gap serves as a quantitative measure of the system's topological protection at E. Specifically, when perturbing the system $H \to H + \delta H$, ζ_E is guaranteed by Weyl's inequality to be preserved so long as $\|\delta H\| < \mu_{(0,0,E)}(X, Y, H)$ [70,71]. In addition, as locations where $\mu_{(x,y,E)} = 0$ are associated with the locations of a system's states [72], changes in a system's topological marker necessarily imply changes in the structure of its states. A detailed mathematical discussion of Eq. (8), its essential properties, and its relation to atomic limits is given in Appendixes A 5–A 7. In particular, Examples A 3 and A 4 show the form of the two different classes of atomic limits distinguished by ζ_E. Altogether, the use of the operation ρ has facilitated the the translation of physical symmetries to matrix symmetries, enabling us to derive an energy-resolved invariant for classifying fragile topology based on results from matrix homotopy.

III. APPLICATION TO A FOUR-BAND MODEL

Having derived a classification framework applicable to finite systems, we demonstrate its use in a four-band model that is a low-energy approximation of TBG and exhibits fragile topology [28,31]. This model consists of a bilayer honeycomb lattice, as schematically shown in Fig. 1(a), where t_1 and t_2 represent the intra- and interlayer hopping amplitudes, respectively. The blue lines spirally connecting interlayer sites represent next-nearest-neighbor (NNN) hoppings with the hopping phase $\pm\phi$, which can induce a nontrivial fragile band gap. The explicit expression of the Hamiltonian for this lattice

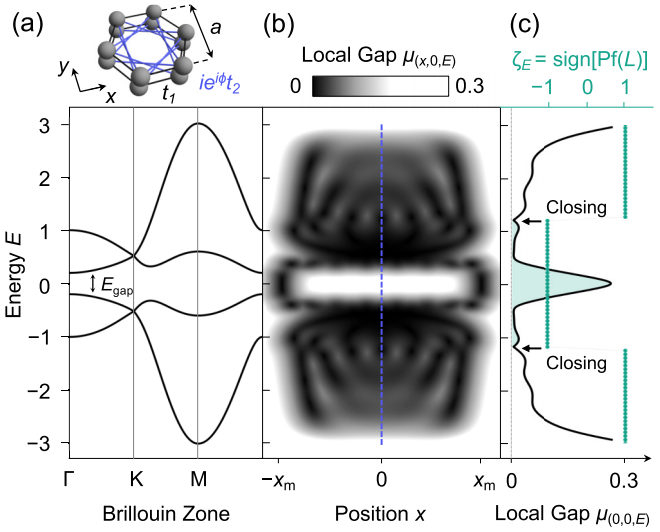

FIG. 1. (a) Bulk band structure for the $C_2\mathcal{T}$-symmetric TBG model. Inset diagrams this lattice model. (b) The local gap $\mu_{(x,y,E)}$ for x and E at $y = 0$. Position x is scaled in terms of the lattice constant a and x_m denotes the length of the edge from the origin. (c) $\mu_{(x,y,E)}$ for E at the center of rotation denoted by blue dotted line in panel (b). The energy-resolved invariant ζ_E is shown by the green dots, where $\kappa = 0.1t/a$ for all calculations.

model in momentum space is given by

$$h(\vec{k}) = \hat{t}_1 \otimes \left[\left(1 + 2\cos\frac{\sqrt{3}k_x a}{2} \cos\frac{k_y a}{2} \right)\sigma_x + 2\sin\frac{\sqrt{3}k_x a}{2}\cos\frac{k_y a}{2}\sigma_y \right] + \hat{t}_2 \otimes \mathbf{1}[n(\vec{k}, \phi) + n^*(\vec{k}, \phi)], \tag{10}$$

with

$$n(\vec{k}, \phi) = ie^{i\phi}(e^{i\mathbf{k}\cdot\mathbf{a}_1} + e^{-i\mathbf{k}\cdot\mathbf{a}_2} + e^{i\mathbf{k}\cdot\mathbf{a}_3}), \tag{11}$$

where we employ $\hat{t}_1 = 0.4t\mathbf{1} + 0.6t\tau_z$ and $\hat{t}_2 = 0.1t\tau_x$, meaning intra- and interlayer hopping amplitudes, respectively, as schematically shown by the black and blue lines in Fig. 1(a). Here, t indicates the overall energy scale, $\mathbf{k} = (k_x, k_y)$ is the in-plane momentum, and the primitive vectors are $\mathbf{a}_{1,2} = (\sqrt{3}, \pm 1)a/2$ and $\mathbf{a}_3 = \mathbf{a}_1 - \mathbf{a}_2$. The Pauli matrices $\sigma_{x,y,z}$ and $\tau_{x,y,z}$ represent the sublattice and orbital degrees of freedom, respectively. We consider the additional interlayer hopping phase to be $\phi = 0$ here so that the initial coefficient of the interlayer hoppings is purely imaginary.

In Fig. 1(a), we show the bulk band structure of the four-band model. All four energy bands are symmetric with respect to the Fermi level and each pair of bands exhibits Dirac points at each of the K and K' points throughout the Brillouin zone. These Dirac points are protected by space-time $C_2\mathcal{T}$ inversion symmetry [28], where $\mathcal{T}^2 = \mathbf{1}$ and C_2 denotes a twofold rotation about the z axis. Note though that the system is neither C_2- nor $\mathcal{T}$-symmetric separately. In addition, the valence bands exhibit an obstruction that prohibits their representation by exponentially localized Wannier functions that obey the system's $C_2\mathcal{T}$ symmetry. As this obstruction disappears when

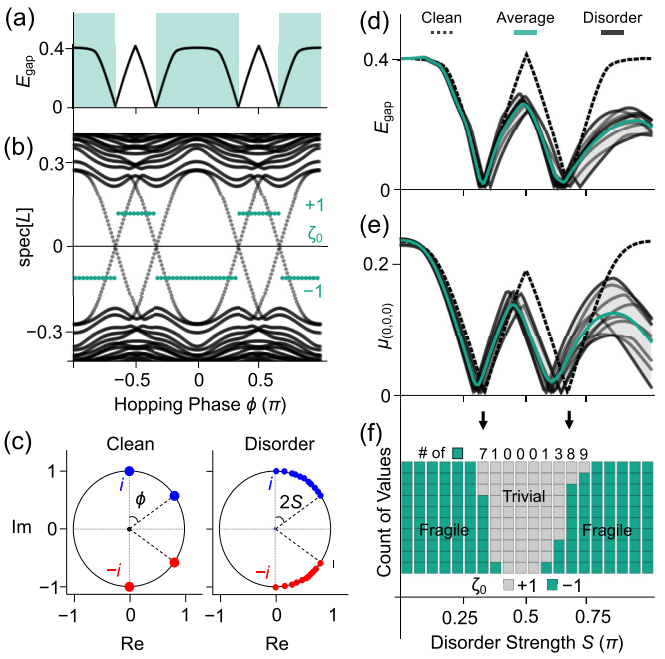

FIG. 2. (a) Closings of E_{gap} due to uniform changes in ϕ in the periodic $C_2\mathcal{T}$-symmetric TBG model. (b) Spectrum of $L_{(0,0,0)}$ (gray) and ζ_0 (green) at the middle of the bulk band gap as ϕ is uniformly varied in the finite TBG system. (c) Hopping phases of clean and disordered systems depicted on the unit circle. The red and blue dots correspond to the opposite off-diagonal terms of the Hamiltonian, forming conjugate pairs. Ensemble analysis of E_{gap} (d), $\mu_{(0,0,0)}$ (e), and histogram of ζ_0 for the ten disorder configurations for increasing S (f). In panels (d) and (e), the black dashed lines show the behavior for uniform hopping phase changes in the clean system. Solid gray lines show the results for each disorder configuration, the solid green line shows the average over the ensemble, and the gray shading fills the area between the maximum and minimum of these data, representing the sample deviations. The histogram in panel (f) uses green and gray to indicate $\zeta_0 = -1$ and $+1$, respectively.

more trivial bands are added to the model, this system exhibits fragile topology [28,31].

To study finite geometries and disorder in the four-band TBG model, we instead work with the system's expression in position space, which is given by the Hamiltonian

$$H = \sum_{\langle i,j\rangle} c_i^\dagger (\hat{t}_1)_{ij} c_j + \sum_{\langle\langle i,j\rangle\rangle} c_i^\dagger s_{ij} (ie^{i\phi}\hat{t}_2)_{ij} c_j, \qquad (12)$$

where $s_{ij} = +1$ is chosen for $\mathbf{r}_i = \mathbf{r}_j + a\mathbf{y}$.

Comparison of the bulk band structure of the infinite four-band TBG model with the local gap of a finite system confirms that the locations in (x, y, E) space with $\mu_{(x,y,E)} \approx 0$ indicate the presence of states at the specified energies and positions [see Figs. 1(a) and 2(b)]. For choices of E residing within the spectral extent of the bulk bands, extended Bloch states are distributed throughout the system and $\mu_{(x,y,E)} \approx 0$ for any choice of (x, y), whereas within the bulk band gap, only localized states exist at the system's boundaries. Note that the fluctuations of $\mu_{(x,0,E)}$ that only intermittently touch zero near the system's boundary in the band gap inherently suggest the weak topological nature of this fragile system; strong topological phases instead exhibit a spheroid of appropriate dimension on which $\mu_{(x,y,E)} = 0$ (see Appendix A 7).

Within the bulk band gap, the energy-resolved marker ζ_E confirms the finite system's fragile topology, while the large local gap at the rotation center indicates this phase's strong topological protection [see Fig. 1(c)]. For energies above and below the bulk gap, ζ_E maintains a nontrivial value of -1 until the first closing points where $\mu_{(0,0,E)} = 0$, beyond which it switches to $+1$. The exact energy where $\mu_{(0,0,E)} = 0$ and ζ_E switches sign varies slightly over a large range of κ (see Appendix C), which may be related to an energy where band inversion has occurred. Although fragile topological phases do not generally exhibit a bulk-boundary correspondence [18–21], our framework reveals a "bulk-boundary-in-energy" correspondence for fragile phases as closings of the local gap guarantee the presence of a nearby state [72] and ζ_E must become trivial for E above or below all four bands.

To confirm that the local fragile marker ζ_E captures phase transitions, we uniformly vary ϕ between all NNN sites from $-\pi$ to π. As can be seen in Fig. 2(a), the width of the bulk spectral gap under this alteration is symmetric about $\phi = 0$ and touches zero at $\phi = \pm\pi/3$ and $\phi = \pm 2\pi/3$. Similarly, the local gap closes at precisely the same points where $E_{\text{gap}} = 0$ and ζ_E changes, indicating a change in the material's fragile topological phase.

As our framework works directly with a finite system expressed in position space, it can inherently be applied to disordered and aperiodic systems. To illustrate this capability, we consider an ensemble of disordered variants of the four-band TBG model where the hopping phases ϕ_{jk} between each pair of NNN sites j and k are randomly assigned a value within an angle range of $2S$ from $\pm i$ from a uniform distribution while preserving $C_2\mathcal{T}$ symmetry. Therefore, S represents the approximate mean value of the disorder strength, allowing us to investigate the phase diagram of the disordered system based on this variable. In Figs. 2(d)–2(f), we present E_{gap}, $\mu_{(0,0,E)}$, and ζ_E as functions of S for ten different disorder realizations. We numerically observe that the disordered samples exhibit spectral gap closings and topological phase transitions near $S = \pi/3$ and $2\pi/3$, confirming our energy-resolved local marker's ability to classify disordered systems.

Moreover, the results in Figs. 2(d)–2(f) provide clear evidence of disorder-induced reentrant phase transitions [61,62] for fragile topology, offering a perspective on the stability of fragile phases. These findings reveal that obstructions to connecting a system to a trivial atomic limit can reemerge beyond a certain disorder threshold rather than simply being destroyed. In particular, such behavior parallels phenomena observed in topological Anderson insulators [73], suggesting an intricate interplay between disorder and topology in moiré systems. Thus, the reentrant topological transition emphasizes the limitations of momentum-space approaches and illustrates the possibilities for a topological marker rooted in a system's position-space description.

IV. APPLICATION TO A 2D PHOTONIC CRYSTAL

Finally, to show the broad applicability of our approach in quantifying material topology across systems described

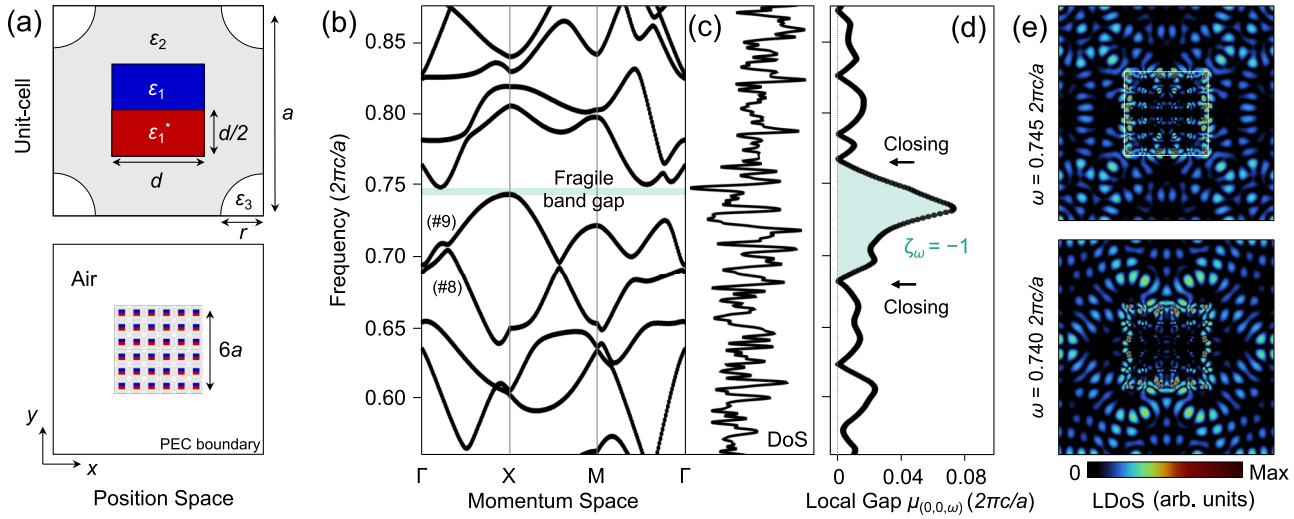

FIG. 3. (a) Schematics of a single unit cell of the photonic crystal (upper) and a heterostructure (lower) formed by 6×6 unit cells surrounded by air bounded by a perfect electrical conductor. Here, $\epsilon_1 = \{16, 6i, 0; -6i, 16, 0; 0, 0, 16\}$, $\epsilon_2 = 4$, $\epsilon_3 = 1$, a is the lattice constant, $r = 0.2a$, and $d = 0.45a$. (b) Band structure of the bulk photonic crystal. The density of states (DoS) (c) and the local gap and frequency-resolved index (d) for the 6×6 finite system from panel (a). Calculations in panel (d) use $\kappa = 0.01\ 2\pi c/a^2$, where c is the speed of light in a vacuum. (e) Local density of states (LDoS) within the fragile band gap depicted by green in panel (b) at the two frequencies for the finite heterostructure shown in panel (a).

by tight-binding and continuum models, the latter of which is traditionally challenging due to high computational costs [74,75], we turn to classifying fragile topology in photonic crystals surrounded by air [76]. We consider the 2D PhC unit-cell structure depicted in Fig. 3(a) that is designed to be $C_2\mathcal{T}$-symmetric, with $\mathcal{T}^2 = \mathbf{1}$, while not exhibiting either symmetry in isolation. The full heterostructure consists of a region containing 6×6 unit cells surrounded by air with perfect electric conductor (PEC) boundary conditions. The system is discretized with standard finite-difference methods to define the Hamiltonian and position operators [69,76–78] and we focus on its transverse electric (TE) modes with nonzero electromagnetic field components (H_z, E_x, E_y).

For the infinite PhC system, the bulk band structure [Fig. 3(b)] possesses two bands that can be shown to exhibit fragile topology using Wilson loops (see Appendix D). However, the inclusion of the surrounding air region in the finite heterostructure removes any spectral gap from the system's DoS, as shown in Fig. 3(c). Nevertheless, the frequency-resolved marker ζ_ω identifies this frequency range as possessing fragile topology despite the lack of a spectral gap [see Fig. 3(d)]. Moreover, although the bulk band gap above the fragile bands is small, the relatively large local gap indicates that the system's topology is more robust than would be suggested by the narrow width of the bulk band gap. The LDoS for the magnetic field intensity near the frequencies of the fragile band gap is shown in Fig. 3(e). At both frequencies inside the fragile band gap, the LDoS is localized at the boundaries of the PhC and has substantial support outside of the PhC. Therefore, these results confirm that our framework for classifying fragile topology can be applied to systems that lack a bulk spectral gap without alteration and that these systems can still exhibit topological robustness associated with the region responsible for the fragile topology.

V. CONCLUSION

In conclusion, we have introduced a position-space framework for classifying fragile topology rooted in matrix homotopy that distinguishes systems based on which atomic limits they can be continued to. Applying this framework to the TBG lattice model and PhC continuum model, we have shown the breadth of the local marker's ability to capture systems' fragile nature. Moreover, the versatility of our method is highlighted by its ability to identify nontrivial fragile phases under conditions of strong disorder and gapless environments. Taking disorder-induced reentrant fragile topology, which is unpredictable by conventional methods, as an example, our approach highlights further opportunities for potential applications across various fields such as strongly correlated materials, metamaterials, and topological photonics. More broadly, the physically motivated arguments we use to derive ζ_E should be extendable to other physical dimensions through a suitable choice of Clifford representation and spectral localizer. Likewise, we expect our approach to be straightforwardly generalizable to other spatial symmetries that square to the identity, as well as extendable to arbitrary spatial symmetries using recent results from field of real C^*-algebras [79].

ACKNOWLEDGMENTS

K.Y.L. and S.W. acknowledge support from the Laboratory Directed Research and Development program at Sandia National Laboratories. S.V. acknowledges support from the U.S. Office of Naval Research (ONR) Multidisciplinary University Research Initiative (MURI) under Grant No. N00014-20-1-2325 on Robust Photonic Materials with Higher-Order Topological Protection. T.A.L. acknowledges support from the National Science Foundation, Grant No. DMS-2349959. A.C. acknowledges support from the U.S. Department of

Energy, Office of Basic Energy Sciences, Division of Materials Sciences and Engineering. This work was performed in part at the Center for Integrated Nanotechnologies, an Office of Science User Facility operated for the U.S. Department of Energy (DOE) Office of Science. Sandia National Laboratories is a multimission laboratory managed and operated by National Technology & Engineering Solutions of Sandia, LLC, a wholly owned subsidiary of Honeywell International, Inc., for the U.S. DOE's National Nuclear Security Administration under Contract No. DE-NA-0003525. The views expressed in the article do not necessarily represent the views of the U.S. DOE or the U.S. Government.

DATA AVAILABILITY

No data were created or analyzed in this study.

APPENDIX A: DERIVING THE INVARIANT FOR CLASSIFYING FRAGILE TOPOLOGY

The main text provides a derivation of a topological marker for classifying fragile topology using results from matrix homotopy. However, underpinning this entire derivation is a real C^*-algebra and associated techniques. Thus, here, as we provide further details on the argument given in the main text, we will also place these arguments into the context of the study of real C^*-algebras.

Broadly, a (complex) C^*-algebra is an associative algebra with a norm and an involution that acts as an adjoint operation. (An involution is an operation that is its own inverse.) For the purposes of this Appendix, it suffices to simply consider the algebra formed by all of the $n \times n$ matrices over the complex field (i.e., matrices whose entries can be complex numbers), $\mathbf{M}_n(\mathbb{C})$, with the usual operations like matrix multiplication, the conjugate transpose $M \mapsto M^\dagger$, in conjunction with the operator norm $\|\cdot\|$ that denotes the largest singular value of the matrix. This example of a C^*-algebra is particularly pertinent to physics, as it is the algebra that contains the physical observables on a finite Hilbert space of dimension n. [However, note that $\mathbf{M}_n(\mathbb{C})$ also contains matrices that are not Hermitian.] Regarding the naming of these algebras, the $*$ in C^*-algebra is $\dagger$ in physics, but we cannot call these $C^\dagger$-algebras so the nomenclature will clash with the notation. A real C^*-algebra possesses a second involution, $M \mapsto M^\rho$, that endows the algebra and its constituent elements with additional structure. For our purposes here of classifying fragile topology, this second involution is built from the symmetries that protect the system's fragile topology.

1. Symmetries

Consider a square system with open boundary conditions (OBCs). This means we have two position observables X and Y and Hamiltonian H. If the system has sides of length L, then $-L/2 \leqslant X \leqslant L/2$ and $-L/2 \leqslant Y \leqslant L/2$ (i.e., all of the eigenvalues of X and Y fall within this range). We will assume that X and Y commute as one assumes in materials science that different positions observables are compatible. For simplicity, we now assume that we have single-particle model on finite-dimensional Hilbert space $\mathfrak{H}$ and that this is a model of a closed system. Thus, we make the assumption that H is a Hermitian matrix $H = H^\dagger$. Finally, we expect some manner of locality, at least strong enough to imply $\|[H, X]\| \leqslant \delta$ and $\|[H, Y]\| \leqslant \delta$ for some $\delta > 0$ that seems small relative to the energy and length scales in the system (e.g., the lattice constants in the two directions and bulk spectral gap).

Fragile topology is generally associated with a system being symmetric with respect to the combination of a spatial symmetry and time reversal. Here, we consider a time-reversal operator $\mathcal{T}$ that is antilinear and squares to $+I$ (spinless models) or to $-I$ (models incorporating spin). Moreover, we also want there to be a unitary operator C_2 that implements rotation by 180°. We will have $C_2^2 = I$ and assume C_2 is real (it is usually a permutation matrix). To keep the antilinear operators visually distinct from the familiar linear operators, we will use caligraphic font to denote such operators and proper composition notation—○—where antiunitary operators are involved.

Altogether, we consider here models where H has $C_2 \circ \mathcal{T}$ symmetry but may lack either C_2 symmetry and/or $\mathcal{T}$ symmetry. Thus, we introduce the composite operator

$$\mathcal{R} = C_2 \circ \mathcal{T}, \tag{A1}$$

which will be an antiunitary symmetry, and our main assumption is

$$H \circ \mathcal{R} = \mathcal{R} \circ H. \tag{A2}$$

Position and time should be independent, so we assume that $\mathcal{T}$ commutes with X and Y. As C_2 is rotation by a half-turn, we assume that R anticommutes with both of these position operators. Thus, we assume

$$\mathcal{R} \circ X = -X \circ \mathcal{R} \text{ and } \mathcal{R} \circ Y = -Y \circ \mathcal{R}. \tag{A3}$$

For the remainder, we will concentrate solely on the spinless case. Further, we assume that time reversal is the standard choice of complex conjugation, i.e.,

$$\mathcal{T}(\mathbf{v}) = \overline{\mathbf{v}} \tag{A4}$$

is a standing assumption from here on. We will also use the notation $\mathcal{K}(\mathbf{v}) = \overline{\mathbf{v}}$ when convienient.

2. Antiunitary symmetries and real C^*-algebras

To understand the distance from a given system to an atomic limit, we will need the mathematical techniques developed using real C^*-algebras over a series of papers from last decade [80–82]. The relevant real C^*-algebra here is the algebra of all $2n \times 2n$ matrices $\mathbf{M}_{2n} = \mathbf{M}_{2n}(\mathbb{C})$, with an involution operation similar to the transpose that is built from $\mathcal{R}$. We will use $\top$ to denote transpose, so $M^\dagger = \overline{M^\top} = \overline{M}^\top$.

To give $\mathbf{M}_{2n}$ a real structure, we define a generalized involution $M \mapsto M^\rho$ by

$$M^\rho = \mathcal{R}^{-1} \circ M^\dagger \circ \mathcal{R}.$$

Since we have $\mathcal{R} \circ \mathcal{R} = I$, this simplifies to $M^\rho = \mathcal{R} \circ M^\dagger \circ \mathcal{R}$. Recall that $\mathcal{R} = \mathcal{T} \circ C_2 = C_2 \circ \mathcal{T}$. Since $\mathcal{T}$ denotes conjugation, we have $\mathcal{R}(\mathbf{v}) = C_2\overline{\mathbf{v}}$. Therefore,

$$\mathcal{R} \circ M^\dagger \circ \mathcal{R}(\mathbf{v}) = \mathcal{R}\big(M^\dagger C_2 \overline{\mathbf{v}}\big) = C_2 \overline{M^\dagger C_2 \overline{\mathbf{v}}} = C_2 M^\top C_2 \mathbf{v}$$

and we find

$$M^\rho = C_2 M^\top C_2. \tag{A5}$$

That is, this extra operation that creates a real structure for $\mathbf{M}_{2n}$ is the transpose intertwined with a rotation.

Remark A1. Let us look at the very special case where the Hilbert space is $\mathbf{C}^2$. If there are two sites where rotation takes one location to the other, then C_2 is

$$C_2 = \begin{bmatrix} 0 & 1 \\ 1 & 0 \end{bmatrix}.$$

The ρ operation becomes

$$\begin{bmatrix} a & b \\ c & d \end{bmatrix}^\rho = \begin{bmatrix} d & b \\ c & a \end{bmatrix}. \tag{A6}$$

Instead, if there is one site at the fixed point, say with two orbitals, then C_2 will be

$$C_2 = \begin{bmatrix} 1 & 0 \\ 0 & 1 \end{bmatrix},$$

and the ρ operation becomes the standard transpose

$$\begin{bmatrix} a & b \\ c & d \end{bmatrix}^\rho = \begin{bmatrix} a & c \\ b & d \end{bmatrix}. \tag{A7}$$

It is easy to forget how these behave differently and that the second case shows up as a subsystem whenever the full system has a site at the center of rotation.

One axiom for real C^*-algebras is that the generalized involution, here ρ, needs to commute with the adjoint. We know C_2 is Hermitian, so from Eq. (A5) we derive

$$(M^\rho)^\dagger = C_2\big(M^\top\big)^\dagger C_2 = C_2\big(M^\dagger\big)^\top C_2 = \big(M^\dagger\big)^\rho.$$

Considering again a 2D system with Hamiltonian H and position operators X and Y, in real C^*-algebra terminology, we are assuming we have three Hermitian matrices, with X and Y commuting and H almost commuting with the other two, with the symmetry assumptions

$$X^\rho = -X, \quad Y^\rho = -Y, \quad \text{and} \quad H^\rho = H. \tag{A8}$$

To clarify the symmetry on H, we have

$$H = \mathcal{R} \circ H \circ \mathcal{R} \Rightarrow H = (H^\dagger)^\rho \Rightarrow H = H^\rho$$

since H is assumed to be Hermitian.

Definition A1. Suppose $\mathcal{S}$ is an antiunitary symmetry on a Hilbert space $\mathfrak{H}$. A triple of operators (X, Y, H) on $\mathfrak{H}$ is said to have $\mathcal{S}^{(-,-,+)}$*symmetry* if they are all Hermitian and

$$\mathcal{S} \circ X = -X \circ \mathcal{S}, \quad \mathcal{S} \circ Y = -Y \circ \mathcal{S} \quad \text{and } \mathcal{S} \circ H = H \circ \mathcal{S}\,.$$

3. Converting from a standard physics setting to a standard math setting

In a basis-free sense, any antiunitary that squares to $+I$ is equivalent to any other. Computer modeling of a physical system, however, needs to be done in a fixed basis. To avoid decimating our physical intuition, we want to select those basis vectors so that they correspond to a single location. To be able to utilize centuries of work in linear algebra, we want to work in a basis where we can work with the standard transpose and not $M \mapsto M^\rho$.

For our computer algorithms, we will need an explicit unitary so that conjugation by that unitary converts $M \mapsto M^\top$ back to $M \mapsto M^\rho$. This is essentially as described in Sec. 2 of Ref. [83], but this is an easy calculation, so we include it here for completeness.

Lemma A1. Suppose R is real, unitary, and $R^2 = I$. Define

$$M^\tau = R M^\top R.$$

Let

$$W = \frac{1}{\sqrt{2}}(R + iI).$$

This is unitary, and for any matrix M we have

$$(WMW^\dagger)^\top = W M^\tau W^\dagger.$$

Proof. The conditions on R imply $R^\top = R$ and $R^\dagger = R$. To see W is unitary, we calculate

$$2W^\dagger W = (R - iI)(R + iI) = 2I.$$

Note that $W^\top = W$ and so $\overline{W} = W^\dagger$. Also,

$$iRW^\dagger = \frac{1}{\sqrt{2}} iR(R - iI) = W.$$

The main calculation is then

$$(WMW^\dagger)^\top = W^\dagger M^\top W = WRM^\top RW^\dagger = WM^\tau W^\dagger.$$

■

For working with the given physical system, we need a fixed W, namely,

$$W = \frac{1}{\sqrt{2}}(C_2 + iI). \tag{A9}$$

This is our choice to intertwine the two symmetry pictures, meaning

$$(WMW^\dagger)^\top = W M^\rho W^\dagger. \tag{A10}$$

Indeed, there are other choices for W to achieve this intertwining and we need a fixed choice to get a well-defined local topological invariant.

The basic observables in the physical models we wish to study will be triples in the following set:

$$\mathcal{M}_\epsilon(\mathcal{R}, 2n) = \Bigg\{ (X, Y, H) \in (\mathbf{M}_{2n})^3 \times \begin{vmatrix} (X, Y, H) \text{ is } \mathcal{R}^{(-,-,+)}\text{-symmetric} \\ \|[H, X]\| \leqslant \epsilon, \ \|[H, Y]\| \leqslant \epsilon \\ L(X, Y, H) \text{ is invertible} \end{vmatrix} \Bigg\}. \tag{A11}$$

If the Hamiltonian actually commutes with position, then $(X, Y, H) \in \mathcal{M}_0(\mathcal{R}, 2n)$ is an *atomic limit* in this class of models.

After a change of basis, so conjugation of everything by W, this set becomes the following:

$$\mathcal{M}_\epsilon(\mathcal{K}, 2n) = \Big\{ (X, Y, H) \in (\mathbf{M}_{2n})^3 \times \begin{vmatrix} (X, Y, H) \text{ is } \mathcal{K}^{(-,-,+)}\text{-symmetric} \\ \|[H, X]\| \leqslant \epsilon, \ \|[H, Y]\| \leqslant \epsilon \\ L(X, Y, H) \text{ is invertible} \end{vmatrix} \Big\}. \tag{A12}$$

Except for how the relevant matrices act on vectors, these two sets have identical structure. They are isometric as metric spaces, for example.

In Eqs. (A11) and (A12), $L(X, Y, H)$ refers to the spectral localizer formed from the triplet of matrices. This operator will be formally introduced in Appendix A 4.

4. The commutative case to model atomic limits—part I

A system is in an *atomic limit* if the Hamiltonian commutes with all of the position observables. This shuts down hopping terms between any neighboring sites, so an excitation at a site evolves as if the other sites do not exist. (Different orbitals at the same lattice site can still be coupled in an atomic limit.) In the next subsection, we classify all such commuting, locally gapped systems, i.e., elements of $\mathcal{M}_0(\mathcal{R}, 2n)$. Here, we first examine the structure of $\mathcal{M}_0(\mathcal{K}, 2n)$.

We need to understand the structure of three commuting Hermitian matrices, two of which are purely imaginary and the third is real. [Again, as $\mathcal{K}$ is just complex conjugation, and (X, Y, H) is $\mathcal{K}^{(-,-,+)}$-symmetric in $\mathcal{M}_0(\mathcal{K}, 2n)$, the position operators are purely imaginary. This is not physically relevant in this form, but it is a convenient basis to explore some of the mathematics.] As such, we need work with a real version of the spectral theorem, and identify an invariant that makes sense for a mix of real and imaginary matrices.

Theorem A1. If $N_1, \ldots, N_k$ are commuting normal real $n \times n$ matrices, then there is a real orthogonal matrix U, of determinant one, so that

$$N_j = U D_j U^\dagger,$$

with each D_j block diagonal, with every block either 1×1 and real or a 2×2 block of the form

$$\begin{bmatrix} a & -b \\ b & a \end{bmatrix},$$

with a and b real.

Proof. Except for the requirement on the determinant of U, this can be found on p. 292, Theorem 12, of Ref. [84]. It also follows easily from the version of the Schur decomposition that applies to commuting real normal matrices. If $\det(U) = -1$, then we can multiply its first row by -1, and multiply the first row and column of each X_j by -1, to get this factorization with the determinant of orthogonal matrix having the opposite sign. ■

Theorem A2. If X, Y, and H are commuting $2n \times 2n$ Hermitian matrices, with X and Y purely imaginary and H real, then there is a real orthogonal matrix U of determinant one so that

$$X = U X_D U^\dagger, \quad Y = U Y_D U^\dagger, \quad H = U H_D U^\dagger,$$

where H_D is a real diagonal matrix, and X_D and Y_D are block diagonal with 2×2 blocks of the form

$$\begin{bmatrix} 0 & -ib \\ ib & 0 \end{bmatrix}, \tag{A13}$$

with b real.

Proof. Notice that iX, iY, and H are normal and real. Applying Theorem A1 to these three provides a unitary U of norm one so that

$$iX = U X_1 U^\dagger, \quad iY = U Y_1 U^\dagger, \text{ and } H = U H_D U^\dagger,$$

with H_D being real and diagonal, and X_1 and Y_1 being real block diagonal with blocks of the form

$$\begin{bmatrix} a & -b \\ b & a \end{bmatrix}.$$

Since H is Hermitian, H_D will be Hermitian. Let $X_D = -iX_1$ and $Y_D = -iY_1$. Since iX and iY are anti-Hermitian, the blocks of X_1 and Y_1 will be anti-Hermitian. The blocks of X_D and Y_D will be Hermitian and purely imaginary, so will be of the form in Eq. (A13). ■

In Eq. (A12), we noted that the spectral localizer for (X, Y, H) must be invertible. We now pin down the choice of the γ_j in the definition of the spectral localizer in $\mathcal{M}_\epsilon(\mathcal{K}, 2n)$. We use the Pauli spin matrices in a specific order and so we will use the convention

$$L(X, Y, H) = X \otimes \sigma_x + Y \otimes \sigma_z + H \otimes \sigma_y.$$

With this convention, $L(X, Y, H)$ will be skew-symmetric (as well as Hermitian) and so has a well-defined Pfaffian. The sign of this Pfaffian is a natural invariant. The fact that the spectral localizer is skew-symmetric forces its eigenvalues to appear in pairs $\pm\alpha$. The spectral localizer is $4n \times 4n$, so there will be an even number of pairs and so its determinant will be positive. This implies that its Pfaffian will be real, so the sign makes sense.

More generally, we define

$$L_{(x,y,E)}(X, Y, H) = (X - x) \otimes \sigma_x + (Y - y) \otimes \sigma_z + (H - E) \otimes \sigma_y. \tag{A14}$$

Only if $x = y = 0$ do we retain the symmetries needed to give us a skew-symmetric localizer, so our local invariant is only defined at the center of rotation.

Small examples show that the Pfaffian can come out positive or negative. The sign of the Pfaffian cannot change along a path in $\mathcal{M}_\epsilon(\mathcal{K}, 2n)$ since we have excluded the case where the spectral localizer is singular.

Remark A2. A $2n \times 2n$ matrix M that is both Hermitian and skew-symmetric must have spectrum whose eigenvalues come in pairs $\pm\lambda$ [65,85]. Two invertible Hermitian, skew-symmetric matrices H_0 and H_1 can be connected by a path of invertible Hermitian, skew-symmetric matrices if and only if $\mathrm{Pf}(H_0)$ and $\mathrm{Pf}(H_1)$ are of the same sign. Given a path H_t of Hermitian, skew-symmetric matrices, the sign of $\mathrm{Pf}(H_t)$ can only change when $\mathrm{Pf}(H_t) = \pm\sqrt{(\det(H_t))}$ is zero. This means

the sign of $\mathrm{Pf}(H_t)$ can only change when a pair of eigenvalues crosses 0 in opposite directions.

Example A1. For any real α, β, and γ, consider the matrices

$$X = \begin{bmatrix} 0 & -i\alpha \\ i\alpha & 0 \end{bmatrix}, \quad Y = \begin{bmatrix} 0 & -i\beta \\ i\beta & 0 \end{bmatrix}, \quad H = \begin{bmatrix} \gamma & 0 \\ 0 & \gamma \end{bmatrix}.$$

These commute, are Hermitian, with the first two antisymmetric and the last symmetric. We find

$$L(X,Y,H) = \begin{bmatrix} 0 & -i\beta & -i\gamma & -i\alpha \\ i\beta & 0 & i\alpha & -i\gamma \\ i\gamma & -i\alpha & 0 & i\beta \\ i\alpha & i\gamma & -i\beta & 0 \end{bmatrix},$$

whose Pfaffian is always positive, as it equals

$$(-i\beta)(i\beta) - (-i\gamma)(-i\gamma) + (-i\alpha)(i\alpha) = \alpha^2 + \beta^2 + \gamma^2.$$

Since

$$\begin{aligned}(L(X,Y,H))^2 &= \left(X^2 + Y^2 + H^2\right) \otimes I_2 \\ &= (\alpha^2 + \beta^2 + \gamma^2) \otimes I_4,\end{aligned}$$

this must have spectrum contained in the set $\{\pm(\alpha^2 + \beta^2 + \gamma^2)\}$. Every skew-symmetric, Hermitian matrix has spectrum that is symmetric across 0, so both eigenvalues must have multiplicity two. In particular, $L(X,Y,H)$ is invertible so long as at least one of α, β, or γ is nonzero.

Example A2. For any real numbers γ_j, consider the matrices

$$X = \begin{bmatrix} 0 & 0 \\ 0 & 0 \end{bmatrix}, \quad Y = \begin{bmatrix} 0 & 0 \\ 0 & 0 \end{bmatrix}, \quad H = \begin{bmatrix} \gamma_1 & 0 \\ 0 & \gamma_2 \end{bmatrix}. \tag{A15}$$

As the off-diagonal elements are set to zero, these commute. Trivially, X and Y are purely imaginary, and H is real. All are Hermitian. Now we find that $L(X,Y,H)$ can have negative Pfaffian, as it equals

$$-(-i\gamma_1)(-i\gamma_2) = \gamma_1\gamma_2.$$

We find that $L(X,Y,H)$ is invertible so long as γ_j are both nonzero. Indeed, its spectrum is $\{\pm\gamma_1, \pm\gamma_2\}$.

Now we show that the sign of the Pfaffian is the only obstruction to connecting two triples in $\mathcal{M}_0(\mathcal{K}, 2n)$.

Proposition A1. If (X_1, Y_1, H_1) and (X_2, Y_2, H_2) are in $\mathcal{M}_0(\mathcal{K}, 2n)$, then these are connected by a path in $\mathcal{M}_0(\mathcal{K}, 2n)$ if and only if

$$\mathrm{sign}(\mathrm{Pf}(L(X_1, Y_1, H_1)) = \mathrm{sign}(\mathrm{Pf}(L(X_2, Y_2, H_2)).$$

Proof. Since $\mathrm{SU}(n)$ is connected, we can assume both triples are block diagonal. In each 2×2 common block, the triple looks like

$$\begin{bmatrix} 0 & -i\alpha \\ i\alpha & 0 \end{bmatrix}, \quad \begin{bmatrix} 0 & -i\beta \\ i\beta & 0 \end{bmatrix}, \quad \begin{bmatrix} \gamma_1 & 0 \\ 0 & \gamma_2 \end{bmatrix}.$$

The commutativity assumption implies that either $\alpha = \beta = 0$ or $\gamma_1 = \gamma_2$. The blocks with $\gamma_1 = \gamma_2$ can all be connected by a path of such blocks to the special case where $\alpha = \beta = 0$. Thus, we can assume $X = Y = 0$ and H is diagonal.

Any common block of the form

$$\begin{bmatrix} 0 & 0 \\ 0 & 0 \end{bmatrix}, \quad \begin{bmatrix} 0 & 0 \\ 0 & 0 \end{bmatrix}, \quad \begin{bmatrix} -1 & 0 \\ 0 & -1 \end{bmatrix}$$

is homotopic to

$$\begin{bmatrix} 0 & 0 \\ 0 & 0 \end{bmatrix}, \quad \begin{bmatrix} 0 & 0 \\ 0 & 0 \end{bmatrix}, \quad \begin{bmatrix} 1 & 0 \\ 0 & 1 \end{bmatrix},$$

as we see from the path

$$\begin{bmatrix} 0 & 0 \\ 0 & 0 \end{bmatrix}, \quad \begin{bmatrix} 0 & -i\sin\theta \\ i\sin\theta & 0 \end{bmatrix}, \quad \begin{bmatrix} \cos\theta & 0 \\ 0 & \cos\theta \end{bmatrix}.$$

Since

$$\begin{bmatrix} 0 & -1 \\ 1 & 0 \end{bmatrix}\begin{bmatrix} 1 & 0 \\ 0 & -1 \end{bmatrix}\begin{bmatrix} 0 & 1 \\ -1 & 0 \end{bmatrix}^\dagger = \begin{bmatrix} -1 & 0 \\ 0 & 1 \end{bmatrix}$$

and

$$\begin{bmatrix} 0 & -1 \\ 1 & 0 \end{bmatrix}$$

is homotopic to I_2 in $\mathrm{SO}(2)$, we can assume blocks all look like 0, 0 followed by

$$\begin{bmatrix} 1 & 0 \\ 0 & -1 \end{bmatrix} \text{ or } \begin{bmatrix} 1 & 0 \\ 0 & 1 \end{bmatrix}.$$

Similarly,

$$\begin{bmatrix} 0 & 0 & -1 & 0 \\ 0 & 1 & 0 & 0 \\ 1 & 0 & 0 & 0 \\ 0 & 0 & 0 & 1 \end{bmatrix}\begin{bmatrix} -1 & 0 & 0 & 0 \\ 0 & 1 & 0 & 0 \\ 0 & 0 & -1 & 0 \\ 0 & 0 & 0 & 1 \end{bmatrix}\begin{bmatrix} 0 & 0 & -1 & 0 \\ 0 & 1 & 0 & 0 \\ 1 & 0 & 0 & 0 \\ 0 & 0 & 0 & 1 \end{bmatrix}^\dagger$$
$$= \begin{bmatrix} 1 & 0 & 0 & 0 \\ 0 & 1 & 0 & 0 \\ 0 & 0 & 1 & 0 \\ 0 & 0 & 0 & 1 \end{bmatrix},$$

so we can assume there is at most one block with opposite signs. We can use a unitary of determinant one to swap that block around, so every triple is homotopic to either $(0, 0, I)$ or $(0, 0, D)$, where D is diagonal with all diagonal elements equal to 1 except the top-left element that is equal to -1. ■

5. The commutative case to model atomic limits—part II

With these results in hand for the nonphysical $\mathcal{M}_\epsilon(\mathcal{K}, 2n)$, we are in a position to translate these results to the physically meaningful $\mathcal{M}_\epsilon(\mathcal{R}, 2n)$.

Definition A2. Suppose (X, Y, H) is an element $\mathcal{M}_\epsilon(\mathcal{R}, 2n)$. We define the spectral localizer as

$$\begin{aligned}L_{(x,y,E)}(X,Y,H) = (X - xI) \otimes \sigma_x + (Y - yI) \otimes \sigma_z \\ + (H - EI) \otimes \sigma_y,\end{aligned}$$

and when $x = y = 0$, we can define a local invariant, taking values in $\{1, -1\} \cong \mathbb{Z}_2$,

$$\begin{aligned}&\zeta_E(X,Y,H) \\ &\quad = \mathrm{sign}\left(\mathrm{Pf}\left(L_{(x,y,E)}\left(WXW^\dagger, WYW^\dagger, WHW^\dagger\right)\right)\right),\end{aligned} \tag{A16}$$

where W is as defined in Eq. (A9). This is defined whenever the local Clifford gap is nonzero and $x = y = 0$, where the local Clifford gap is defined as

$$\mu^{\mathrm{C}}_{(x,y,E)}(X,Y,H) = \sigma_{\min}(L_{(x,y,E)}(X,Y,H)),$$

i.e., the smallest singular value of the spectral localizer.

In passing, we note that a more aesthetically pleasing formula would be

$$\zeta_E(X,Y,H) = \mathrm{sign}(\mathrm{Pf}((W\otimes I)L_{(0,0,E)}(X,Y,H)(W\otimes I)^\dagger)). \quad \text{(A17)}$$

However, the formula in Eq. (A16) will generally yield a slightly faster numerical algorithm.

We now consider a pair of examples to again show how $\zeta_E(X,Y,H)$ can take values of both ± 1.

Example A3. Assume we have just two distinct sites that are swapped by rotation, at locations $(\pm\alpha, \pm\beta)$ with $\alpha \neq 0$ or $\beta \neq 0$. If

$$X = \begin{bmatrix} -\alpha & 0 \\ 0 & \alpha \end{bmatrix}, \quad Y = \begin{bmatrix} -\beta & 0 \\ 0 & \beta \end{bmatrix}, \quad H = \begin{bmatrix} \gamma & 0 \\ 0 & \gamma \end{bmatrix},$$

then $WXW^\dagger$, $WYW^\dagger$, and $WHW^\dagger$ are the matrices discussed in Example A 1. These form a triple in $\mathcal{M}_0(\mathcal{R}, 2)$ and so

$$\zeta_E(X,Y,H) = 1$$

for any $E \neq \gamma$.

Example A4. Let

$$X = \begin{bmatrix} 0 & 0 \\ 0 & 0 \end{bmatrix}, \quad Y = \begin{bmatrix} 0 & 0 \\ 0 & 0 \end{bmatrix}, \quad H = \begin{bmatrix} \alpha & -i\beta \\ i\beta & \alpha \end{bmatrix}.$$

These constitute a triple in $\mathcal{M}_0(\mathcal{R}, 2)$. We find

$$WXW^\dagger = \begin{bmatrix} 0 & 0 \\ 0 & 0 \end{bmatrix}, \quad WYW^\dagger = \begin{bmatrix} 0 & 0 \\ 0 & 0 \end{bmatrix},$$
$$WHW^\dagger = \begin{bmatrix} \alpha+\beta & 0 \\ 0 & \alpha-\beta \end{bmatrix}$$

and so

$$\zeta_E(X,Y,H) = \mathrm{sign}((\alpha+\beta-E)(\alpha-\beta-E)).$$

This equals -1 for E between $\alpha-\beta$ and $\alpha+\beta$.

6. Connecting to an Atomic limit

We discussed earlier that two locally gapped, $C_2\mathcal{T}$-symmetric systems of different invariant cannot be connected by a continuous path of such systems. Here, we discuss a possible converse. We already know that atomic limits of the same invariant can be connected, so will attempt to show that every locally gapped $C_2\mathcal{T}$-symmetric system can be connected to an atomic limit where this limit system is also locally gapped and $C_2\mathcal{T}$-symmetric. A complication arises: if the starting system (X_0, Y_0, H_0) is in $\mathcal{M}_\epsilon(\mathcal{R}, 2n)$ and (X_1, Y_1, H_1) is that atomic limit, we cannot expect (X_t, Y_t, H_t) to stay in $\mathcal{M}_\epsilon(\mathcal{R}, 2n)$. Instead, we hope to prove that (X_t, Y_t, H_t) stays in $\mathcal{M}_\delta(\mathcal{R}, 2n)$, where δ is a bit larger than ϵ.

Here, we offer only a sketch of a possible argument. The estimates of how large δ will be will depend on both ϵ and the size of the local gap. We anticipate that soon someone will develop rigorous results about paths to commuting matrices with these symmetries, for both open boundary conditions and periodic boundary conditions (PBCs). The recent advances [86] in matrix approximations that respect antilinear and linear symmetries should work in this setting. Earlier work, not involving antilinear symmetries, indicates that this approximation only works when the "joint spectrum" of the given matrices is two dimesional [87]. It is for this reason we start with spectral flattening.

There are at least two ways to define a local gap of system (X, Y, H). The quadratic gap is the square root of the smallest singular value of

$$Q(X,Y,Z) = X^2 + Y^2 + H^2,$$

while the Clifford gap is the smallest singular value of

$$L(X,Y,H) = \begin{bmatrix} H & X - iY \\ X + iY & -H \end{bmatrix}.$$

The Clifford gap at zero is denoted by $\mu_{(0,0,0)}(X,Y,H)$ in the main text. Since $L(X,Y,H)$ is an approximate square root of an amplification of $Q(X,Y,H)$, these two notions of local gap are approximately equal.

The goal of the spectral flattening is to gain the approximate relation that makes this an approximate representation of a sphere. We expect this reduction to help, as many related commuting-matrix approximation problems require at most a two-dimensional "joint spectrum" [87].

Suppose we are given (X,Y,H) in $\mathcal{M}_\epsilon(\mathcal{R}, 2n)$. Beyond insisting that $L(X,Y,H)$ is invertible, lets assume

$$g^2 \leqslant (L(X,Y,H))^2 \leqslant G^2,$$

where $2\epsilon < g < G$. Then,

$$g^2 - 2\epsilon \leqslant X^2 + Y^2 + H^2 \leqslant G^2 + 2\epsilon.$$

The usual spectral flatting adjusts only H, replacing it with $\tilde{H} = H(H^2)^{-1/2}$. We cannot do this here, as open boundary conditions mean there is no sizable gap expected in our H and so the commutator of $\tilde{H}$ with X and Y will likely blow up. Instead, we define

$$Q = X^2 + Y^2 + H^2$$

and then

$$X_t = Q^{-t/4} X Q^{-t/4}, \quad Y_t = Q^{-t/4} Y Q^{-t/4},$$
$$H_t = Q^{-t/4} H Q^{-t/4}.$$

These are continuous paths of Hermitian matrices. We next check that we still have $C_2\mathcal{T}$ symmetry. We can show, by polynomial approximation to the square-root function, that $(Q^{-t/4})^\rho = (Q^\rho)^{-t/4}$ and so

$$(Q^{-t/4})^\rho = (X^2 + Y^2 + H^2)^{-t/4} = Q^{-t/4}.$$

Given this, it is easy to show that

$$X_t^\rho = -X_t^\rho, \quad Y_t^\rho = -Y_t^\rho, \quad H_t^\rho = H_t^\rho.$$

Again using polynomial approximation, one can show that

$$\|[H_t, X_t]\| \leqslant \delta, \quad \|[H_t, Y_t]\| \leqslant \delta,$$

where δ is larger than ϵ but only depends on ϵ and g. See Theorem 3.2.32 of Ref. [88]. Thus, (X_t, Y_t, H_t) is a continuous path in $\mathcal{M}_\delta(\mathcal{R}, 2n)$. Since

$$X_t^2 \approx Q^{-t/2} X^2 Q^{-t/2},$$

etc., we find

$$(L(X_t, Y_t, H_t))^2 \approx Q^{1-t}.$$

Here, we will need ϵ small compared to g^2 to ensure that (X_t, Y_t, H_t) remains gapped for every t.

At $t = 1$, we have an approximate relation,

$$X_1^2 + Y_1^2 + H_1^2 \approx I.$$

As we explain in Sec. A of Ref. [69], we can map the coordinate functions in $C(S^2)$ to these three matrices and extend to get a map

$$\varphi : C(S^2) \to \boldsymbol{M}_{2n}(\mathbb{C})$$

that behaves somewhat like a $*$-homomorphism. In this case, the real structure $M \mapsto M^\rho$ will correspond to the real structure on $C(S^2)$ induced by a 180° rotation. This is very close to the setting of Ref. [81]. The main result there tells us that two almost commuting real orthogonal matrices are always close to commuting real orthogonal matrices. What we have is a similar mathematical situation, where we replace the role of the two-torus with a rotation by the two-sphere with a rotation. If the following conjecture is correct, we can derive the same result but with $X^\rho = -X$, etc., as we have the unitary W that conjugates one picture to the other.

Conjecture A1. For any $\eta > 0$, there is a $\delta > 0$ such that, for all n, given matrices X_1, Y_1, and H_1 in $\boldsymbol{M}_{2n}(\mathbb{C})$ with

$$X_1^\dagger = X_1 = -\overline{X_1}, \quad Y_1^\dagger = Y_1 = -\overline{Y_1}, \quad H_1^\dagger = H_1 = \overline{H_1}$$

and

$$\|[H_1, X_1]\| \leqslant \delta, \quad \|[H_1, Y_1]\| \leqslant \delta,$$
$$\left\|X_1^2 + Y_1^2 + H_1^2 - I\right\| \leqslant \delta,$$

there is a triple (X_2, Y_2, H_2) of commuting Hermitian matrices, with $X_2^\rho = -X_2$, $Y_2^\rho = -Y_2$, $H_2^\rho = H_2$, $X_2^2 + Y_2^2 + H_2^2 = I$, and

$$\|X_2 - X_1\| \leqslant \eta, \quad \|Y_2 - Y_1\| \leqslant \eta, \quad \|H_2 - H_1\| \leqslant \eta.$$

Assuming this conjecture true, we find that we can find a commuting $C_2\mathcal{T}$-symmetric system (X_2, Y_2, H_2) close to (X_1, Y_1, H_1). As long as η is small, we can linearly interpolate between (X_1, Y_1, H_1) and (X_2, Y_2, H_2) to complete the path. The result is a path of locally gapped, $C_2\mathcal{T}$-symmetric systems with limited growth in the commutators that terminates in an atomic limit. By limited growth, we mean

$$\|[H_t, X]\| \leqslant \frac{2\|[H_t, X]\|}{g}$$

or something similar.

7. Strong versus Fragile topology in the pseudospectrum

The invariant ζ_E differs fundamentally from the local version of the Chern number that looks at

$$C_L(x, y, E) = \tfrac{1}{2}\mathrm{sig}(L_{(x,y,E)}(X, Y, H)).$$

The key difference is that our invariant can only be defined at $x = y = 0$. Because $C_L(x, y, E)$ is not restricted to $x = y = 0$, the Clifford spectrum (points in position-energy space where the local gap is zero) of a Chern insulator is always spherelike. Specifically, if one travels on any ray out of the origin (assuming a local gap at the origin), one will hit at least one point in the Clifford spectrum. In math terms, we say that the Clifford spectrum separates the origin from infinity.

In Fig. 4, we plot a portion near the origin of the $y = 0$ slice of the Clifford pseudospectrum of the tight-binding model considered in the main text next to the same for a Chern insulator (the Haldane model). Of particular importance is the portion that is completely black. This set is called the Clifford spectrum. At first glance, the black parts in both plots look spherelike, but a close look reveals a difference. The black region in Fig. 4(b) does not entirely enclose the origin; one can see separation between some of the black dots. Indeed, we suspect that the unusual spectral flattening discussed in Appendix A 6 may not be necessary. That is, the speckled look of the Clifford pseudospectrum seems to indicate that the TBG tight-binding model is already close to an atomic limit.

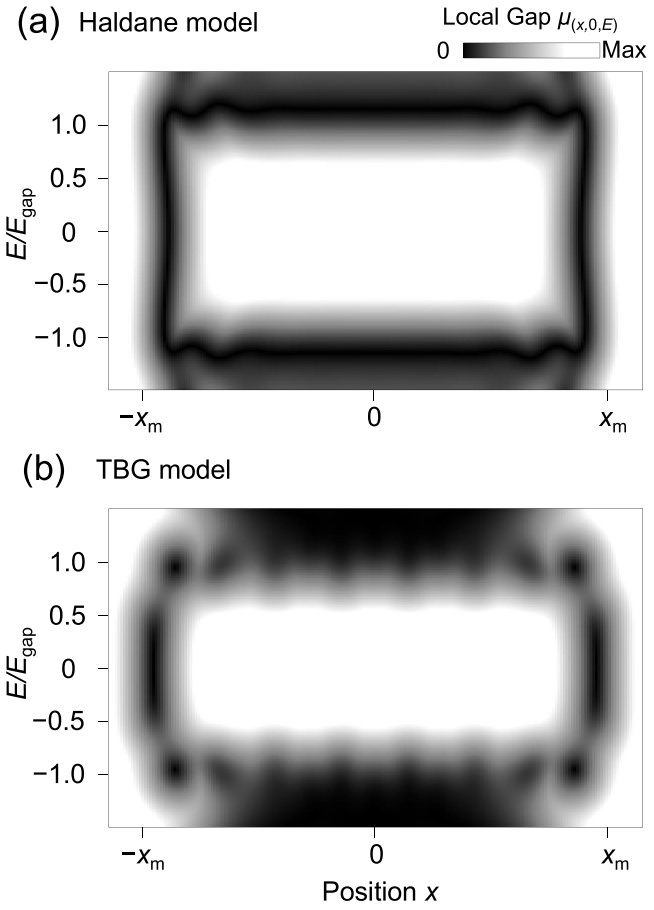

FIG. 4. Clifford pseudospectrum—strong vs fragile topology. Comparison of the Clifford pseudospectrum between models of a Chern insulator and a fragile insulator. (a) A standard Haldane model of a Chern insulator, with local gap shown along the slice $y = 0$. (b) The TBG tight-binding model considered in main text, same slice shown of the local gap. The blackest region in each is Clifford spectrum, where the local gap is zero. In panel (a), we see a slice of a spherelike region that completely surrounds the position-energy origin $(x, y, E) = (0, 0, 0)$. In panel (b), the black region does not completely enclose the origin.

Local invariants that detect other strong invariants, at least in classes A, AI, and AII, also force the Clifford spectrum to separate the origin from infinity. For example, see Fig. 9.8 in Ref. [66] for a horizontal slice ($E = 0$) of a spin-Chern insulator. For a three-dimensional example in class AII, see Fig. 10.1 in Ref. [66], where now the image is only for $z = E = 0$. For a four-dimensional example in class AI, see Fig. 7.1 in Ref. [89]. In all cases, the Clifford spectrum has a

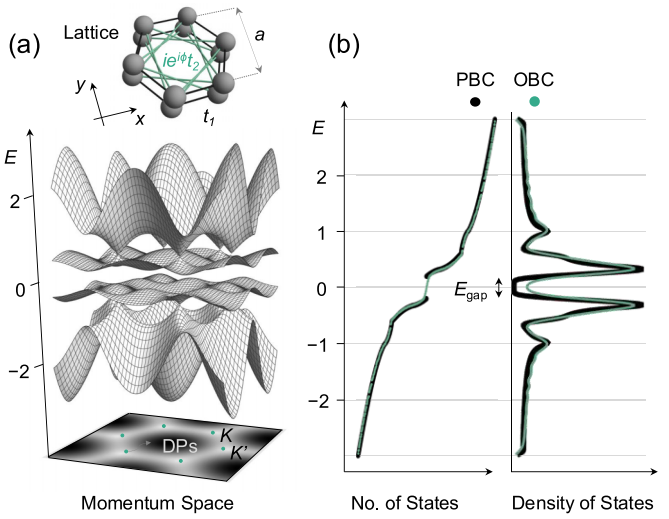

FIG. 5. Twisted bilayer graphene morié lattice model and its characteristic features. (a) Schematic representation for the unit-cell lattice and the calculated band structure. The band gap width is denoted by E_{gap} and Dirac points are shown at the K and K'. High-symmetry points are $\Gamma = (0, 0)$, $M = (2\pi/\sqrt{3}a, 0)$, and $K = (2\pi/\sqrt{3}a, 2\pi/3a)$. (b) Energy eigenvalues for the number of states and its density of states under periodic and open boundary conditions. Here, t is an overall energy scale.

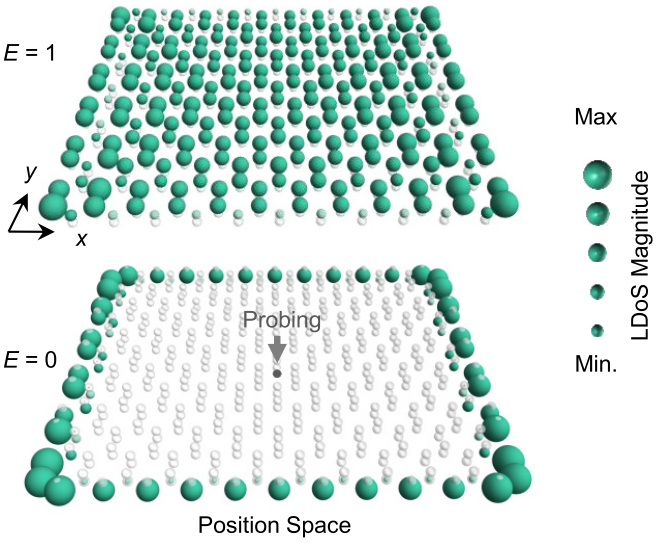

FIG. 6. LDoS of the finite TBG model. LDoS within ($E = 0$) and outside ($E = t$) the bulk band gap. The magnitude of the LDoS at specific energies is represented by the size of the green spheres at each lattice sites.

portion that surrounds the origin like a sphere, and this feature is stable under perturbations within the symmetry class.

8. An explanation via *K* theory

The formula in Equation (A16) for the invariant ζ_0 could have been deduced from Theorem 4.5 of Ref. [90]. That theorem is about explicit generators of the various KO and KU groups of $C(S^2 \setminus \{\mathbf{np}\}, \sigma)$, where σ is the rotation by 180° that fixes the removed North pole **np** and the South pole. This tells us that $L(\hat{x}, \hat{y}, \hat{z})$ is a unitary with the correct symmetries to represent a generator of

$$KO_2(C(S^2 \setminus \{\mathrm{np}\}, \sigma)),$$

so long as the γ matrices are chosen correctly. Here, $\hat{x}$ and so forth are the coordinate functions restricted to the sphere. Notice, however, that all the formulas in this table look like a localizer of the coordinate functions with varying choices of γ matrices. As such, it is often possible to guess the needed index formulas, just by seeking the minimum size γ matrices that have the needed symmetries so the spectral localizer will end up with the expected symmetries.

To get an invariant out of an element of a KO group of $C(S^d)$ with some symmetry, we just replace the coordinate functions with the matrix observables and arrive at an invertible element in $\mathbf{M}_n(\mathbb{C})$ with some antiunitary symmetry. (In some cases, more than one antiunitary symmetry is involved.) Since the target algebra does not change as we change dimensions and symmetry class, all these invariants (so far) end up with one of three calculations, the signature, sign of a determinant, or sign of a Pfaffian. The mathematical formalism here involves universal C^*-algebras, as explained in Sec. 3 of Ref. [91]. Fortunately, one can understand why these indices can only change when the local gap closes without this abstraction; none of the signature, sign of a determinant, or sign of a Pfaffian can change without an eigenvalue first becoming zero as the spectral localizer is Hermitian (for Hermitian systems).

There are explicit generators of KO groups calculated in Ref. [83] for different symmetries on the two-sphere, and research on this is ongoing. It is anticipated that pseudospectral methods to create local topological invariants will work with antiunitary symmetries that commute with some of the position observables and anticommute with others, and either commute or anticommute with the Hamiltonian.

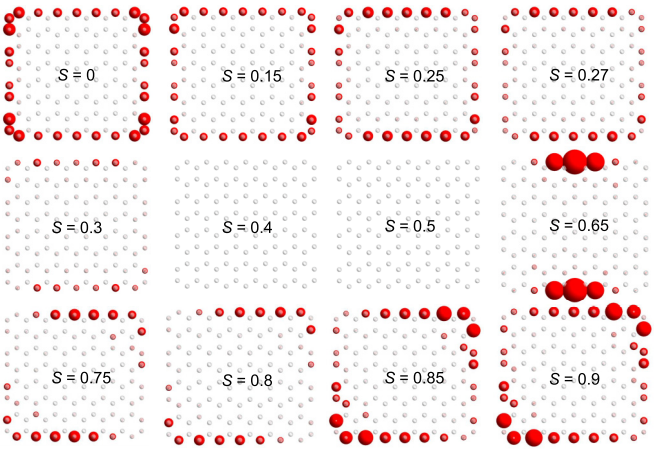

FIG. 7. LDoS for the TBG model at $E = 0$ with $C_2\mathcal{T}$-symmetry-preserving disorder. Each plot shows the LDoS for a single disorder configuration for each selected disorder strength S.

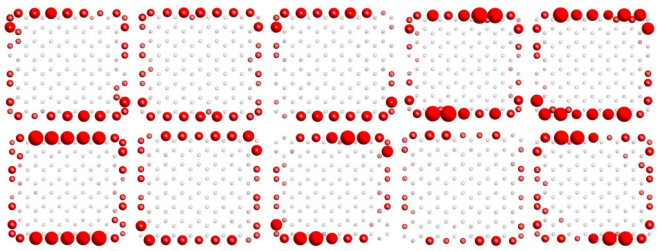

FIG. 8. Susceptible nature of the TBG boundary states due to the effects of disorder. LDoS at $E = 0$ and $S = 0.85$ for ten different disorder samples.

APPENDIX B: THE TBG LATTICE MODEL, EDGE STATES, AND THE EFFECTS OF DISORDER

In this section, we present calculations of edge states arising in the open boundary TBG model given in Eq. (10). In Fig. 5(a), we show the bulk band structure of the four-band model. Moreover, we show the energy spectra and density of states of Eq. (12) under periodic and open boundary conditions in Fig. 5(b), which are well matched except in the bulk band gap. Under PBC, there is a band gap corresponding to $E_{\text{gap}} = 0.4t$, whereas under OBC, the spectrum becomes gapless due to the presence of trivial edge states [21,49,92] (see this Appendix).

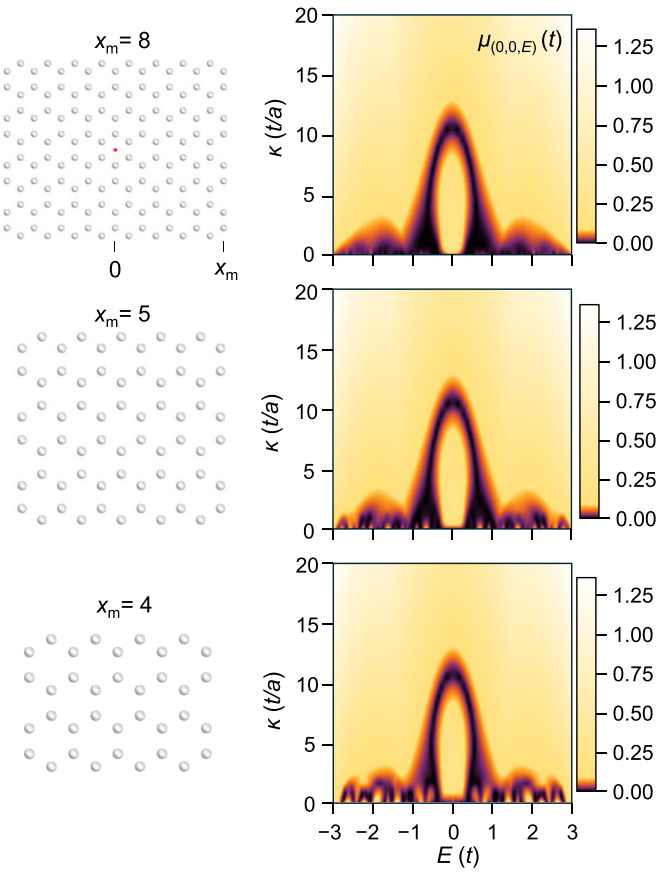

FIG. 9. Consistency of the local gap in the κ-energy domain with respect to changes in total system size.

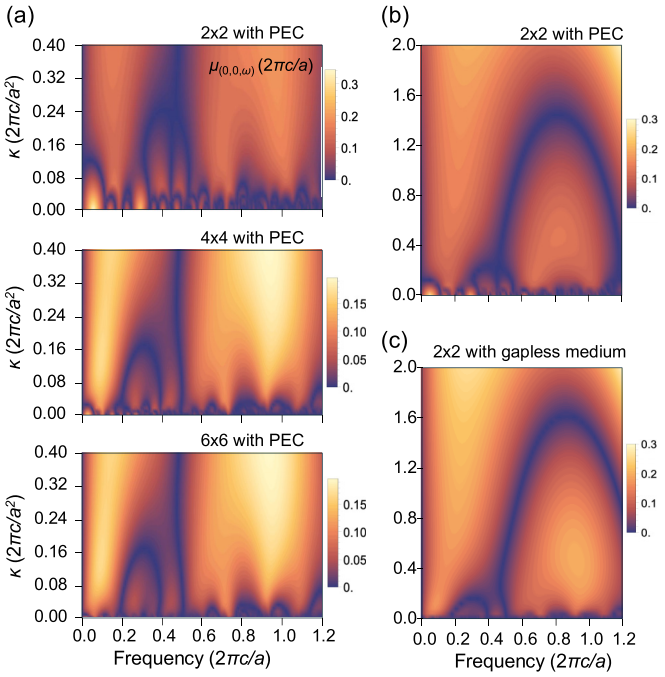

FIG. 10. Consistency of the local gap behavior in the κ-frequency domain with respect to changes in total system size and the environment. (a) Local gap μ calculation results for 2×2, 4×4, and 6×6 with PEC boundaries. Large-scale view of local gap μ calculation results for 2×2 with PEC boundary (b) and surrounded by air (c).

In Fig. 6, we show the LDoS calculations for two energies of the TBG model with open boundaries. The magnitude of the LDoS at each site is represented by the size of the green spheres. Unlike the LDoS at $E = t$ within the bulk bands, which is uniform across the entire system, the LDoS at $E = 0$ within the band gap is localized along the system boundary. As discussed in the main text, these trivial edge states are susceptible to disorder, in contrast to those that arise from strong and stable topology such as chiral edge states in Chern insulators. Figure 7 shows the evolution of the LDoS at $E = 0$ as the disorder strength S increases (using the same definition of this parameter from the main text). Note that the localized edge states, which are uniformly distributed along the system boundary in the clean system ($S = 0$), become unevenly distributed as S increases. These edge states disappear as the system enters the trivial phase within a certain range of S, and reappear with the reentrant fragile topological phase at strong S. Figure 8 shows the LDoS at $E = 0$ for different disorder samples at $S = 0.85$. As clearly shown in this result, the edge states are unevenly distributed along the boundary due to the disorder.

APPENDIX C: A SCALING COEFFICIENT AND SIZE DEPENDENCE OF A LOCAL GAP

Figures 9 and 10 illustrate the calculations of the local gap μ in the κ-energy domain for lattice and continuum models, respectively, indicating that these properties are consistently maintained regardless of the total system size and the surrounding environment. In Fig. 9, the local gap is calculated

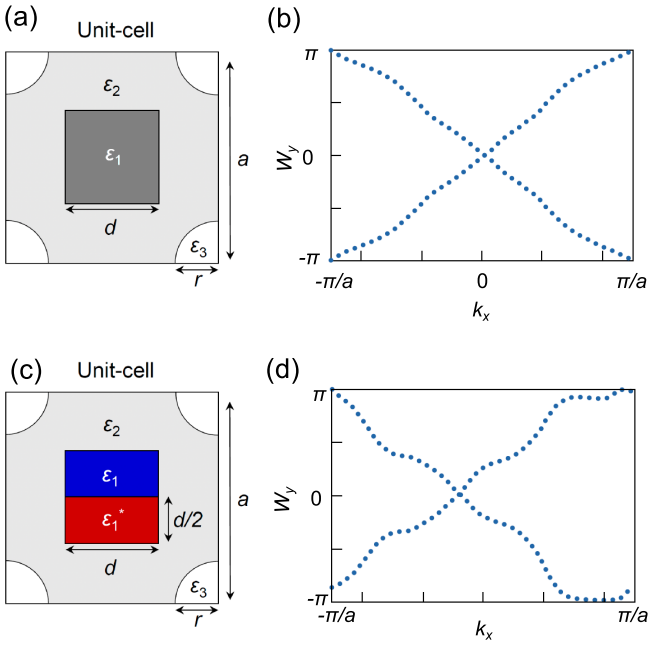

FIG. 11. Wilson loop calculations for photonic crystals with fragile bands. (a) Unit cell of the photonic crystal with both C_2 and $\mathcal{T}$ symmetries. Here, $\epsilon_1 = 16$, $\epsilon_2 = 4$, and $\epsilon_3 = 1$. a is a period, and $r = 0.2a$, $d = 0.4a$, and $G = 2\pi/a$. (b) Wilson loop eigenvalues W_y for the TE-polarized bands 8 and 9, plotted as a function of k_x. The winding of the eigenvalues indicates the non-Wannierizablility of the bands. The crossing of the eigenvalues at $k_x = 0$ and π is enforced by C_2 symmetry. (c) Unit cell of the photonic crystal with $C_2\mathcal{T}$ but with individually broken C_2 and $\mathcal{T}$ symmetries. Here, ϵ_1 is the anisotropic permittivity tensor given in the main text, $\epsilon_2 = 4$, and $\epsilon_3 = 1$. a is a period, and $r = 0.2a$, $d = 0.45a$, and $G = 2\pi/a$. (d) Wilson loop eigenvalues W_y for the TE-polarized bands 8 and 9, plotted as a function of k_x. Under $C_2\mathcal{T}$ symmetry, the winding in the spectrum is retained and the crossing of the eigenvalues is stable. However, the crossing can occur at arbitrary k_x.

within the energy range from -3 to $+3$ and κ from 0 to $20t/a$. Considering the shift in homotopy invariant upon touching $\mu = 0$, it is evident that μ robustly protects the topology near the bulk band gap at $E = 0$. This topological phase becomes trivialized after the local gap touches zero near $\kappa = 12t/a$ as κ increases. Note that the local gap behavior in the κ-E domain remains consistent despite changes in the spatial size of the lattice, with $x_m = 8$, 5, and 4. Similarly, Fig. 10 presents calculations of the local gap for the continuum model. Figure 10(a) shows the results for three different unit-cell counts under PEC boundary conditions. Figure 10(b) demonstrates the results at larger κ scales for the PEC and air boundaries. These results confirm the consistency of the spectral localizer framework through the large local gap values near the fragile band gap and the qualitative agreement in the κ-ω domain.

APPENDIX D: WILSON LOOPS FOR PHOTONIC CRYSTALS WITH FRAGILE BANDS

A standard momentum-space method for characterizing band topology is to compute the Wilson loop spectrum. The Wilson loop operator over a closed loop l is given by

$$\mathcal{W}_{m,n} = \mathcal{P}\exp\left(i\oint_l \mathbf{A}_{m,n}(\mathbf{k})\cdot d\mathbf{k}\right), \tag{D1}$$

where $\mathbf{A}_{m,n}(\mathbf{k}) = \langle u_{m,\mathbf{k}}|i\nabla_{\mathbf{k}}u_{n,\mathbf{k}}\rangle$ is the Berry connection defined over the space-periodic part of the eigenstates of interest, $u_{m,\mathbf{k}}(\mathbf{r})$. The Wilson loop operator is a matrix that encodes the geometric phases traced by eigenstates along closed loops in momentum space. Specifically, the eigenvalues of $\mathcal{W}$ represent the Berry phases accumulated along the loop. A nontrivial winding in the Wilson loop eigenvalue spectrum signifies the non-Wannierizability of the bands, indicating their nontrivial topology. In the case of photonic crystals, this calculation can be performed using the electromagnetic eigenmodes extracted from finite-element or plane-wave expansion methods [52,55,64].

Here, we calculate the Wilson loop spectra for the PhC structures studied in the main text. We compute the eigenvalues of $\mathcal{W}$ along noncontractible paths in momentum space with a fixed k_y and plot them as a function of k_x. First, let us consider the PhC with the unit cell shown in Fig. 11(a) with both C_2 and $\mathcal{T}$ symmetries. The Wilson loop spectrum for TE-polarized bands 8 and 9 is shown in Fig. 11(b). We observe a double winding of the eigenvalues in the spectrum indicating that these bands are fragile. Moreover, the crossings at $k_x = 0$ and π are enforced by the presence of C_2 symmetry. In Fig. 11(c), we consider the PhC studied in the main text with broken C_2 and $\mathcal{T}$ symmetries but with preserved $C_2\mathcal{T}$. The corresponding Wilson loop spectrum shown in Fig. 11(d) continues to exhibits a double winding of the eigenvalues indicating fragile topology. However, under $C_2\mathcal{T}$, these crossings are generic and can occur at arbitrary k_x [25,29,32].

We emphasize that this momentum-space method is only valid for infinite, spatially periodic structures and fails in the presence of boundaries, gapless environments, or disorder. Furthermore, position-space symmetry indicators, which can identify fragile topology, require spatial symmetries that are absent in the $C_2\mathcal{T}$ structure considered above [57]. In contrast, the position-space methods introduced in the main text are applicable to gapless and finite heterostructures, such as those shown in Fig. 4(d), as well as to systems with disorder, as illustrated in Fig. 3.

[1] F. D. Haldane, Model for a quantum Hall effect without Landau levels: Condensed-matter realization of the "parity anomaly", Phys. Rev. Lett. **61**, 2015 (1988).

[2] C. L. Kane and E. J. Mele, Z_2 topological order and the quantum spin Hall effect, Phys. Rev. Lett. **95**, 146802 (2005).

[3] M. Hafezi, A. S. Sørensen, E. Demler, and M. D. Lukin, Fractional quantum Hall effect in optical lattices, Phys. Rev. A **76**, 023613 (2007).

[4] N. Regnault and B. A. Bernevig, Fractional Chern insulator, Phys. Rev. X **1**, 021014 (2011).

[5] E. J. Bergholtz and Z. Liu, Topological flat band models and fractional Chern insulators, Int. J. Mod. Phys. B **27**, 1330017 (2013).

[6] Z. Liu and E. J. Bergholtz, Recent developments in fractional Chern insulators, in *Encyclopedia of Condensed Matter Physics*, 2nd ed., edited by T. Chakraborty (Academic Press, Oxford, 2024), pp. 515–538.

[7] H. Park, J. Cai, E. Anderson, Y. Zhang, J. Zhu, X. Liu, C. Wang, W. Holtzmann, C. Hu, Z. Liu *et al.*, Observation of fractionally quantized anomalous Hall effect, Nature (London) **622**, 74 (2023).

[8] J. Léonard, S. Kim, J. Kwan, P. Segura, F. Grusdt, C. Repellin, N. Goldman, and M. Greiner, Realization of a fractional quantum Hall state with ultracold atoms, Nature (London) **619**, 495 (2023).

[9] P. Törmä, S. Peotta, and B. A. Bernevig, Superconductivity, superfluidity and quantum geometry in twisted multilayer systems, Nat. Rev. Phys. **4**, 528 (2022).

[10] J. Yu, B. A. Bernevig, R. Queiroz, E. Rossi, P. Törmä, and B.-J. Yang, Quantum geometry in quantum materials, arXiv:2501.00098.

[11] Z.-D. Song and B. A. Bernevig, Magic-angle twisted bilayer graphene as a topological heavy fermion problem, Phys. Rev. Lett. **129**, 047601 (2022).

[12] A. Kitaev, Periodic table for topological insulators and superconductors, AIP Conf. Proc. **1134**, 22 (2009).

[13] A. P. Schnyder, S. Ryu, A. Furusaki, and A. W. Ludwig, Classification of topological insulators and superconductors in three spatial dimensions, Phys. Rev. B **78**, 195125 (2008).

[14] S. Ryu, A. P. Schnyder, A. Furusaki, and A. W. Ludwig, Topological insulators and superconductors: Tenfold way and dimensional hierarchy, New J. Phys. **12**, 065010 (2010).

[15] L. Fu, Topological crystalline insulators, Phys. Rev. Lett. **106**, 106802 (2011).

[16] J. Kruthoff, J. De Boer, J. Van Wezel, C. L. Kane, and R. J. Slager, Topological classification of crystalline insulators through band structure combinatorics, Phys. Rev. X **7**, 041069 (2017).

[17] W. A. Benalcazar, B. A. Bernevig, and T. L. Hughes, Quantized electric multipole insulators, Science **357**, 61 (2017).

[18] H. C. Po, H. Watanabe, and A. Vishwanath, Fragile topology and Wannier obstructions, Phys. Rev. Lett. **121**, 126402 (2018).

[19] S. H. Kooi, G. van Miert, and C. Ortix, Classification of crystalline insulators without symmetry indicators: Atomic and fragile topological phases in twofold rotation symmetric systems, Phys. Rev. B **100**, 115160 (2019).

[20] P. Zhu, A. Alexandradinata, and T. L. Hughes, $\mathbb{Z}_2$ spin Hopf insulator: Helical hinge states and returning Thouless pump, Phys. Rev. B **107**, 115159 (2023).

[21] Y.-C. Chen, Y.-P. Lin, and Y.-J. Kao, Stably protected gapless edge states without Wannier obstruction, Phys. Rev. B **107**, 075126 (2023).

[22] B. Bradlyn, L. Elcoro, J. Cano, M. G. Vergniory, Z. Wang, C. Felser, M. I. Aroyo, and B. A. Bernevig, Topological quantum chemistry, Nature (London) **547**, 298 (2017).

[23] H. C. Po, A. Vishwanath, and H. Watanabe, Complete theory of symmetry-based indicators of band topology, Nat. Commun. **8**, 1 (2017).

[24] W. A. Benalcazar, T. Li, and T. L. Hughes, Quantization of fractional corner charge in C^n-symmetric higher-order topological crystalline insulators, Phys. Rev. B **99**, 245151 (2019).

[25] A. Bouhon, A. M. Black-Schaffer, and R. J. Slager, Wilson loop approach to fragile topology of split elementary band representations and topological crystalline insulators with time-reversal symmetry, Phys. Rev. B **100**, 195135 (2019).

[26] H. X. Wang, G. Y. Guo, and J. H. Jiang, Band topology in classical waves: Wilson-loop approach to topological numbers and fragile topology, New J. Phys. **21**, 093029 (2019).

[27] R. Bistritzer and A. H. MacDonald, Moiré bands in twisted double-layer graphene, Proc. Natl. Acad. Sci. USA **108**, 12233 (2011).

[28] J. Ahn, S. Park, and B. J. Yang, Failure of Nielsen-Ninomiya theorem and fragile topology in two-dimensional systems with space-time inversion symmetry: Application to twisted bilayer graphene at magic angle, Phys. Rev. X **9**, 021013 (2019).

[29] Z. Song, Z. Wang, W. Shi, G. Li, C. Fang, and B. A. Bernevig, All magic angles in twisted bilayer graphene are topological, Phys. Rev. Lett. **123**, 036401 (2019).

[30] Y. Hwang, J. Ahn, and B. J. Yang, Fragile topology protected by inversion symmetry: Diagnosis, bulk-boundary correspondence, and Wilson loop, Phys. Rev. B **100**, 205126 (2019).

[31] H. C. Po, L. Zou, T. Senthil, and A. Vishwanath, Faithful tight-binding models and fragile topology of magic-angle bilayer graphene, Phys. Rev. B **99**, 195455 (2019).

[32] B. Bradlyn, Z. Wang, J. Cano, and B. A. Bernevig, Disconnected elementary band representations, fragile topology, and Wilson loops as topological indices: An example on the triangular lattice, Phys. Rev. B **99**, 045140 (2019).

[33] L. Zou, H. C. Po, A. Vishwanath, and T. Senthil, Band structure of twisted bilayer graphene: Emergent symmetries, commensurate approximants, and Wannier obstructions, Phys. Rev. B **98**, 085435 (2018).

[34] D. Călugăru, A. Chew, L. Elcoro, Y. Xu, N. Regnault, Z. D. Song, and B. A. Bernevig, General construction and topological classification of crystalline flat bands, Nat. Phys. **18**, 185 (2022).

[35] Y. Cao, V. Fatemi, A. Demir, S. Fang, S. L. Tomarken, J. Y. Luo, J. D. Sanchez-Yamagishi, K. Watanabe, T. Taniguchi, E. Kaxiras, R. C. Ashoori, and P. Jarillo-Herrero, Correlated insulator behaviour at half-filling in magic-angle graphene superlattices, Nature (London) **556**, 80 (2018).

[36] D. V. Else, H. C. Po, and H. Watanabe, Fragile topological phases in interacting systems, Phys. Rev. B **99**, 125122 (2019).

[37] J. Liu, J. Liu, and X. Dai, Pseudo Landau level representation of twisted bilayer graphene: Band topology and implications on the correlated insulating phase, Phys. Rev. B **99**, 155415 (2019).

[38] A. M. Turner, E. Berg, and A. Stern, Gapping fragile topological bands by interactions, Phys. Rev. Lett. **128**, 056801 (2022).

[39] Y. Cao, V. Fatemi, S. Fang, K. Watanabe, T. Taniguchi, E. Kaxiras, and P. Jarillo-Herrero, Unconventional superconductivity in magic-angle graphene superlattices, Nature (London) **556**, 43 (2018).

[40] S. Peotta and P. Törmä, Superfluidity in topologically nontrivial flat bands, Nat. Commun. **6**, 8944 (2015).

[41] F. Xie, Z. Song, B. Lian, and B. A. Bernevig, Topology-bounded superfluid weight in twisted bilayer graphene, Phys. Rev. Lett. **124**, 167002 (2020).

[42] H. C. Po, L. Zou, A. Vishwanath, and T. Senthil, Origin of Mott insulating behavior and superconductivity in twisted bilayer graphene, Phys. Rev. X **8**, 031089 (2018).

[43] V. Peri, Z. D. Song, B. A. Bernevig, and S. D. Huber, Fragile topology and flat-band superconductivity in the strong-coupling regime, Phys. Rev. Lett. **126**, 027002 (2021).

[44] C. A. Rosiek, G. Arregui, A. Vladimirova, M. Albrechtsen, B. Vosoughi Lahijani, R. E. Christiansen, and S. Stobbe, Observation of strong backscattering in valley-Hall photonic topological interface modes, Nat. Photon. **17**, 386 (2023).

[45] S. Xu, Y. Wang, and R. Agarwal, Absence of topological protection of the interface states in Z_2 photonic crystals, Phys. Rev. Lett. **131**, 053802 (2023).

[46] J. Ding, M. Li, A. B. Khanikaev, and X. Ni, Topology classification in bi-anisotropic topological photonic crystals via the Wilson loop approach [Invited], Opt. Mater. Express **14**, 1995 (2024).

[47] S. J. Palmer and V. Giannini, Berry bands and pseudo-spin of topological photonic phases, Phys. Rev. Res. **3**, L022013 (2021).

[48] V. Peri, Z. D. Song, M. Serra-Garcia, P. Engeler, R. Queiroz, X. Huang, W. Deng, Z. Liu, B. Andrei Bernevig, and S. D. Huber, Experimental characterization of fragile topology in an acoustic metamaterial, Science **367**, 797 (2020).

[49] Y. Wu, Z. K. Lin, Y. Yang, Z. Song, F. Li, and J. H. Jiang, Probing fragile topology with dislocations, Sci. Bull. **69**, 3657 (2024).

[50] J. L. Mañes, Fragile phonon topology on the honeycomb lattice with time-reversal symmetry, Phys. Rev. B **102**, 024307 (2020).

[51] Z. Li, H. C. Chan, and Y. Xiang, Fragile topology based helical edge states in two-dimensional moon-shaped photonic crystals, Phys. Rev. B **102**, 245149 (2020).

[52] S. Vaidya, A. Ghorashi, T. Christensen, M. C. Rechtsman, and W. A. Benalcazar, Topological phases of photonic crystals under crystalline symmetries, Phys. Rev. B **108**, 085116 (2023).

[53] Y. Wang, S. Xu, L. Feng, and R. Agarwal, Design of fragile topological flat bands in an optical microcavity array, Phys. Rev. B **110**, 045401 (2024).

[54] A. Ghorashi, S. Vaidya, M. C. Rechtsman, W. A. Benalcazar, M. Soljačić, and T. Christensen, Prevalence of two-dimensional photonic topology, Phys. Rev. Lett. **133**, 056602 (2024).

[55] M. B. De Paz, M. G. Vergniory, D. Bercioux, A. Garciá-Etxarri, and B. Bradlyn, Engineering fragile topology in photonic crystals: Topological quantum chemistry of light, Phys. Rev. Res. **1**, 032005 (2019).

[56] J. Schulz, S. Vaidya, and C. Jörg, Topological photonics in 3D micro-printed systems, APL Photonics **6**, 080901 (2021).

[57] Z. D. Song, L. Elcoro, and B. Andrei Bernevig, Twisted bulk-boundary correspondence of fragile topology, Science **367**, 794 (2020).

[58] Z. D. Song, L. Elcoro, Y. F. Xu, N. Regnault, and B. A. Bernevig, Fragile phases as affine monoids: Classification and material examples, Phys. Rev. X **10**, 031001 (2020).

[59] B. Lian, F. Xie, and B. A. Bernevig, Landau level of fragile topology, Phys. Rev. B **102**, 041402(R) (2020).

[60] G. F. Lange, A. Bouhon, and R. J. Slager, Spin texture as a bulk indicator of fragile topology, Phys. Rev. Res. **5**, 033013 (2023).

[61] M.-T. Rieder, P. W. Brouwer, and İ. Adagideli, Reentrant topological phase transitions in a disordered spinless superconducting wire, Phys. Rev. B **88**, 060509 (2013).

[62] G.-Q. Zhang, L.-Z. Tang, L. F. Quezada, S.-H. Dong, and D.-W. Zhang, Reentrant topological phases and spin density wave induced by 1D moiré potentials, Commun. Phys. **8**, 275 (2025).

[63] J. Cano, B. Bradlyn, Z. Wang, L. Elcoro, M. Vergniory, C. Felser, M. Aroyo, and B. A. Bernevig, Topology of disconnected elementary band representations, Phys. Rev. Lett. **120**, 266401 (2018).

[64] M. B. de Paz, C. Devescovi, G. Giedke, J. J. Saenz, M. G. Vergniory, B. Bradlyn, D. Bercioux, and A. García-Etxarri, Tutorial: Computing topological invariants in two-dimensional photonic crystals, Adv. Quantum Technol. **3**, 1900117 (2020).

[65] D. Serre, *Matrices: Theory and Applications*, Graduate Texts in Mathematics, 2nd ed. (Springer, New York, 2010), Vol. 216.

[66] T. A. Loring, *K*-theory and pseudospectra for topological insulators, Ann. Phys. **356**, 383 (2015).

[67] T. A. Loring and H. Schulz-Baldes, Finite volume calculation of *K*-theory invariants, New York J. Math. **23**, 1111 (2017).

[68] T. Loring and H. Schulz-Baldes, The spectral localizer for even index pairings, J. Noncommut. Geom. **14**, 1 (2020).

[69] A. Cerjan and T. A. Loring, Classifying photonic topology using the spectral localizer and numerical *K*-theory, APL Photonics **9**, 111102 (2024).

[70] H. Weyl, Das asymptotische Verteilungsgesetz der Eigenwerte linearer partieller Differentialgleichungen (mit einer Anwendung auf die Theorie der Hohlraumstrahlung), Math. Ann. **71**, 441 (1912).

[71] R. Bhatia, *Matrix Analysis*, Graduate Texts in Mathematics (Springer, New York, 1997), Vol. 169.

[72] A. Cerjan, T. A. Loring, and F. Vides, Quadratic pseudospectrum for identifying localized states, J. Math. Phys. **64**, 023501 (2023).

[73] J. Li, R.-L. Chu, J. K. Jain, and S.-Q. Shen, Topological Anderson insulator, Phys. Rev. Lett. **102**, 136806 (2009).

[74] R. Bianco and R. Resta, Mapping topological order in coordinate space, Phys. Rev. B **84**, 241106 (2011).

[75] D. Li, C. Wang, and H. Huang, Real-space approach for the Euler class and fragile topology in quasicrystals and amorphous lattices, SciPost Phys. **17**, 086 (2024).

[76] K. Y. Dixon, T. A. Loring, and A. Cerjan, Classifying topology in photonic heterostructures with gapless environments, Phys. Rev. Lett. **131**, 213801 (2023).

[77] A. Cerjan and T. A. Loring, An operator-based approach to topological photonics, Nanophotonics **11**, 4765 (2022).

[78] A. Cerjan, T. A. Loring, and H. Schulz-Baldes, Local markers for crystalline topology, Phys. Rev. Lett. **132**, 073803 (2024).

[79] J. L. Boersema, The *K*-theory of the sphere with the antipodal involution, arXiv:2506.16612.

[80] T. A. Loring and A. P. Sørensen, Almost commuting unitary matrices related to time reversal, Commun. Math. Phys. **323**, 859 (2013).

[81] T. A. Loring and A. P. Sørensen, Almost commuting orthogonal matrices, J. Math. Anal. Appl. **420**, 1051 (2014).

[82] T. A. Loring and A. P. Sørensen, Almost commuting self-adjoint matrices: The real and self-dual cases, Rev. Math. Phys. **28**, 1650017 (2016).

[83] J. L. Boersema and T. A. Loring, *K*-theory for real C^*-algebras via unitary elements with symmetries, New York J. Math. **22**, 1139 (2016).

[84] F. R. Gantmacher, *Applications of the Theory of Matrices*, translated by J. L. Brenner, D. W. Bushaw and S. Evanusa (Interscience Publishers, Inc., New York, 1959), pp. ix+317.

[85] P. D. Lax, *Linear Algebra and Its Applications*, Pure and Applied Mathematics (Hoboken), 2nd ed. (Wiley-Interscience, Hoboken, NJ, 2007), pp. xvi+376.

[86] D. Herrera, A projection characterization and symmetry bootstrap for elements of a von Neumann algebra that are nearby commuting elements, arXiv:2412.20795.

[87] D. Enders and T. Shulman, Almost commuting matrices, cohomology, and dimension, Ann. Sci. Éc. Norm. Supér. **56**, 1653 (2023).

[88] O. Bratteli and D. W. Robinson, *Operator Algebras and Quantum Statistical Mechanics. C*-and W*-Algebras. Symmetry Groups. Decomposition of States* (Springer Science & Business Media, New York, Heidelberg, 2012), Vol. 1.

[89] A. Cerjan and T. A. Loring, Even spheres as joint spectra of matrix models, J. Math. Anal. Appl. **531**, 127892 (2024).

[90] J. L. Boersema, *K*-theory for real C^*-algebras via unitary elements with symmetries, Part II—Natural transformations and $KO_*(\mathbb{R})$-module operations, Houston J. Math. **46**, 71 (2020).

[91] T. A. Loring *et al.*, Quantitative *K*-theory related to spin Chern numbers, SIGMA **10**, 077 (2014).

[92] M. Fleischmann, R. Gupta, D. Weckbecker, W. Landgraf, O. Pankratov, V. Meded, and S. Shallcross, Moiré edge states in twisted graphene nanoribbons, Phys. Rev. B **97**, 205128 (2018).